

2

WRDC-TR-90-9003  
Volume III

AD-A230 340

**UNIFORM THEORY OF DIFFRACTION  
(UTD) SCATTERING FROM STRUCTURES,  
INCLUDING HIGHER ORDER TERMS**



**Volume III: Technical Overview**

ElectroScience Laboratory  
The Ohio State University  
1320 Kinnear Road  
Columbus, OH 43212

November 1990  
Final Report for Period April 1986 - December 1989

**Approved for Public Release; Distribution is Unlimited**

DTIC  
ELECTE  
DEC 20 1990  
S B D  
Co

Signature Technology Directorate  
Wright Research and Development Center  
Air Force Systems Command  
Wright Patterson Air Force Base, OH 45433-6523

NOTICE

When Government drawings, specifications, or other data are used for any purpose other than in connection with a definitely Government-related procurement, the United States Government incurs no responsibility or any obligation whatsoever. The fact that the government may have formulated or in any way supplied the said drawings, specifications, or other data, is not to be regarded by implication, or otherwise in any manner construed, as licensing the holder, or any other person or corporation; or as conveying any rights or permission to manufacture, use, or sell any patented invention that may in any way be related thereto.

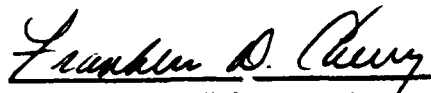
This report is releasable to the National Technical Information Service (NTIS). At NTIS, it will be available to the general public, including foreign nations.

This technical report has been reviewed and is approved for publication.

  
J. EARL JONES, Project Engineer  
Defensive Avionics Division  
Signature Technology Directorate

  
JOSEPH C. FAISON, Chief  
Defensive Avionics Division  
Signature Technology Directorate

FOR THE COMMANDER

  
FRANKLIN D. CHERRY, Director  
Signature Technology Directorate

If your address has changed, if you wish to be removed from our mailing list, or if the addressee is no longer employed by your organization please notify WRDC/SNA, WPAFB, OH 45433-6523 to help us maintain a current mailing list.

Copies of this report should not be returned unless return is required by security considerations, contractual obligations, or notice on a specific document.

REPORT DOCUMENTATION PAGE				Form Approved OMB No. 0704-0188	
1a. REPORT SECURITY CLASSIFICATION UNCLASSIFIED		1b. RESTRICTIVE MARKINGS NONE			
2a. SECURITY CLASSIFICATION AUTHORITY N/A		3. DISTRIBUTION / AVAILABILITY OF REPORT Approved for Public Release; Distribution is Unlimited			
2b. DECLASSIFICATION / DOWNGRADING SCHEDULE N/A					
4. PERFORMING ORGANIZATION REPORT NUMBER(S) 718295-12		5. MONITORING ORGANIZATION REPORT NUMBER(S) WRDC-TR- 90-9003, Vol. III			
6a. NAME OF PERFORMING ORGANIZATION Ohio State University ElectroScience Laboratory		6b. OFFICE SYMBOL (if applicable)	7a. NAME OF MONITORING ORGANIZATION Wright Research and Development Center Signature Technology Directorate (WRDC/SNA)		
6c. ADDRESS (City, State, and ZIP Code) 1320 Kinnear Road Columbus, OH 43212		7b. ADDRESS (City, State, and ZIP Code) Wright-Patterson AFB, OH 45433-6523			
8a. NAME OF FUNDING / SPONSORING ORGANIZATION		8b. OFFICE SYMBOL (if applicable)	9. PROCUREMENT INSTRUMENT IDENTIFICATION NUMBER F33615-86-K-1023		
8c. ADDRESS (City, State, and ZIP Code)		10. SOURCE OF FUNDING NUMBERS			
		PROGRAM ELEMENT NO. 61101F	PROJECT NO. ILIR	TASK NO. A6	WORK UNIT ACCESSION NO. 03
11. TITLE (Include Security Classification) UNIFORM THEORY OF DIFFRACTION (UTD) SCATTERING FROM STRUCTURES, INCLUDING HIGHER ORDER TERMS ; VOLUME III: Technical Overview					
12. PERSONAL AUTHOR(S) Brinkley, Timothy J.; Ivrisimtzis, Leonidas P.; and Marhefka, Ronald J.					
13a. TYPE OF REPORT Final		13b. TIME COVERED FROM APR 86 TO DEC 89	14. DATE OF REPORT (Year, Month, Day) November 1990		15. PAGE COUNT 52
16. SUPPLEMENTARY NOTATION This report volume is Volume III of six volumes.					
17. COSATI CODES			18. SUBJECT TERMS (Continue on reverse if necessary and identify by block number)		
FIELD	GROUP	SUB-GROUP	Uniform Theory of Diffraction (UTD), Geometric Theory of Diffraction (GTD) → Ray Theory, Electromagnetic Scattering, Radar Cross Section, (RCS) → (718295)		
19. ABSTRACT (Continue on reverse if necessary and identify by block number) In this volume, a summary of the basic formulation associated with higher order terms in the theory associated with Uniform Theory of Diffraction (UTD) scattering from structures is presented. Theoretical solutions for bistatic first order and higher order UTD terms, which provide an accurate and efficient means of calculating high frequency scattering from large complex geometries, are discussed. These techniques are eventually incorporated into the user-oriented computer code referred to as the RCS Basic Scattering Code (BSC).					
20. DISTRIBUTION / AVAILABILITY OF ABSTRACT <input checked="" type="checkbox"/> UNCLASSIFIED/UNLIMITED <input type="checkbox"/> SAME AS RPT. <input type="checkbox"/> DTIC USERS			21. ABSTRACT SECURITY CLASSIFICATION Unclassified		
22a. NAME OF RESPONSIBLE INDIVIDUAL J. Earl Jones		22b. TELEPHONE (Include Area Code) (513)-255-9335		22c. OFFICE SYMBOL WRDC/SNA	



<b>Accession For</b>	
NTIS GRA&I	<input checked="" type="checkbox"/>
DTIC TAB	<input type="checkbox"/>
Unannounced	<input type="checkbox"/>
Justification	
By _____	
Distribution/	
<b>Availability Codes</b>	
Dist	Avail and/or Special
A-1	

# Contents

<b>List of Figures</b>	iv
<b>1 Introduction</b>	1
<b>2 Comparison of Methods for Far Zone Scattering from a Flat Plate and Cube</b>	2
2.1 Introduction . . . . .	2
2.2 Theoretical Background . . . . .	3
2.3 Comparisons . . . . .	9
2.4 Discussion . . . . .	18
2.5 Conclusions . . . . .	19
<b>3 Edge Wave Vertex and Edge Diffraction</b>	21
3.1 Introduction . . . . .	21
3.2 Edge Waves . . . . .	22
3.3 The Radiation Integral of the Edge Wave Currents in a Truncated Wedge . . . . .	25
3.4 An Equivalent Current Approach . . . . .	29
3.4.1 Edge Wave Vertex Diffracted Field . . . . .	30
3.4.2 Edge Wave Edge Diffracted Field . . . . .	33
3.4.3 A Heuristic Correction Factor for the Direct Edge Wave	34
3.5 Discussion and Numerical Results . . . . .	35
3.6 Conclusions . . . . .	37
<b>4 Summary</b>	44
<b>Bibliography</b>	45

# List of Figures

2.1	Definition of angles for the Previous Corner Diffraction Coefficients. . . . .	5
2.2	Definition of the Angles used in the New Corner Diffraction Coefficients. . . . .	8
2.3	Two wavelength plate in the x-z plane. . . . .	9
2.4	Backscatter from a 2 wavelength plate ( $\theta = 90^\circ$ pattern). . .	10
2.5	Backscatter from 2 wavelength plate ( $\theta = 90^\circ$ pattern). . .	11
2.6	Backscatter from 2 wavelength plate ( $\theta = 60^\circ$ pattern). . .	11
2.7	Backscatter from a 2 wavelength plate ( $\theta = 60^\circ$ pattern). . .	12
2.8	$2\lambda$ square plate in the x-y plane with a fixed source at $\theta^i = 45^\circ$ and $\phi^i = 0$ . . . . .	13
2.9	Co-polarized RCS in the $\phi = 60^\circ$ plane of a $2\lambda$ square plate with a $\hat{\theta}^i$ polarized fixed source at $\theta^i = 45^\circ$ , $\phi^i = 0^\circ$ . . . . .	13
2.10	Co-polarized RCS in the $\phi = 60^\circ$ plane of a $2\lambda$ square plate with a $\hat{\phi}^i$ polarized fixed source at $\theta^i = 45^\circ$ , $\phi^i = 0^\circ$ . . . . .	14
2.11	Cross-polarized RCS in the $\phi = 60^\circ$ plane of a $2\lambda$ square plate with a $\hat{\theta}^i$ polarized fixed source at $\theta^i = 45^\circ$ , $\phi^i = 0^\circ$ . . . . .	14
2.12	Cross-polarized RCS in the $\phi = 60^\circ$ plane of a $2\lambda$ square plate with a $\hat{\phi}^i$ polarized fixed source at $\theta^i = 45^\circ$ , $\phi^i = 0^\circ$ . . . . .	15
2.13	6" Cube tilted $45^\circ$ in the x-z plane. . . . .	16
2.14	H-plane pattern for 6" cube tilted $45^\circ$ in the x-z plane. . . . .	17
2.15	E-plane pattern for 6" cube tilted $45^\circ$ in the x-z plane. . . . .	17
2.16	RCS for the $\theta = 89^\circ$ cut of a $2\lambda$ square plate with a $\hat{\phi}^i$ polarized fixed source at $\theta^i = 45^\circ$ , $\phi^i = 0^\circ$ . . . . .	19
2.17	RCS for the $\theta = 89^\circ$ cut of a $2\lambda$ square plate with a $\hat{\theta}^i$ polarized fixed source at $\theta^i = 45^\circ$ , $\phi^i = 0^\circ$ . . . . .	20

3.1	Dipole radiating in the close vicinity of the edge of a perfectly conducting wedge. . . . .	23
3.2	Geometry for the edge wave edge and vertex diffraction problem. . . . .	25
3.3	Flat plate geometries examined for the comparison of the calculated field with moment method and measured data: (a) Angular sector, (b) Square plate with the dipole in the center of one of its edges, (c) Rectangular plate with the dipole at unequal distances from the adjacent corners. . . .	39
3.4	Far region edge and vertex diffracted $\hat{\beta}$ -directed field for the angular sector geometry of Fig. 3(a) at the cone $\beta = 85^\circ$ . .	40
3.5	Far field $\hat{\beta}$ -directed wave radiated by the dipole of Fig. 3(b) at the azimuthal cut $\phi = 180^\circ$ . . . . .	41
3.6	Far field $\hat{\beta}$ -directed wave radiated by the dipole of Fig. 3(b) at the azimuthal cut $\phi = 135^\circ$ . . . . .	41
3.7	Far field $\hat{\beta}$ -directed wave radiated by the dipole of Fig. 3(b) at the azimuthal cut $\phi = 45^\circ$ . . . . .	42
3.8	Far field $\hat{\phi}$ -directed wave radiated by the dipole of Fig. 3(b) at the azimuthal cut $\phi = 120^\circ$ . . . . .	42
3.9	Far field $\hat{\beta}$ -directed wave radiated by the dipole of Fig. 3(c) at the azimuthal cut $\phi = 180^\circ$ . <i>Solid line: Calculated field, Dashed line: Measured field, Dotted line: Moment method solution.</i> . . . . .	43
3.10	Far field $\hat{\beta}$ -directed wave radiated by the dipole of Fig. 3(c) at the azimuthal cut $\phi = 150^\circ$ . <i>Solid line: Calculated field, Dashed line: Measured field, Dotted line: Moment method solution.</i> . . . . .	43

# Chapter 1

## Introduction

This volume gives a summary of some of the technical achievements on Contract No. F33615-86-K-1023 .

The overall goals of this contract are to study and determine solutions for bistatic first order and higher order Uniform Geometrical Theory of Diffraction terms, that provide an accurate and efficient means to calculate high frequency scattering from large complex geometries. Algorithms will be developed to incorporate these techniques into a user oriented computer code referred to as the RCS - Basic Scattering Code.

This volume presents parts of two theoretical studies that have been completed. Chapter 2 discusses various methods for determining the first order scattering from flat plate structures. It presents a newly developed far zone corner (vertex) diffraction coefficient. Complete details are given in Volume I. Chapter 3 presents a discussion of a form of edge wave - vertex interaction. It is specifically formulated in this case for a source excitation. This is an intermediate step for determining the far zone edge wave solution. More details are given in Volume II. Other higher order effects are being studied and will be reported on in due course.

## Chapter 2

# Comparison of Methods for Far Zone Scattering from a Flat Plate and Cube

### 2.1 Introduction

The validity of various methods for determining the far zone bistatic scattering from a flat plate and convex flat plate structure such as a cube is presented in this paper. This is accomplished by comparing the methods in various basic situations. The specific techniques to be compared in this study are the classical equivalent currents with "stripping" [3], the previous corner diffraction coefficient [3], the newly developed equivalent currents by Michaeli [4], and an extension to this method cast in the form of a Uniform Geometrical Theory of Diffraction (UTD) far zone corner diffraction coefficient [1]. In addition, the Method of Moments (MOM) using the Electromagnetic Surface Patch (ESP) code [5] and measurements from The Ohio State University ElectroScience Laboratories compact range are used to further validate the results.

A recent paper by Ludwig [6] compares three methods for backscattering from a cube, that is, the MOM using the Numerical Electromagnetics Code (NEC-MOM), physical optics (PO), and the previous UTD corner diffraction solution. In this paper, it will be shown that methods which give comparable results for backscatter can differ for bistatic scattering. The emphasis here is to present basic examples that can be used to val-

update existing codes and to suggest a numerically efficient and accurate method for convex flat plate structures to first order.

An approximate expression for the far zone field scattered by the vertex of a finite perfectly conducting wedge is presented in this regard. The solution is cast in the form of the UTD and is based on asymptotic equivalent currents found using modified PTD concepts [4,1]. The faces of the wedge must be flat (the normal to each individual face is a constant everywhere on the face except at the edge) and the edges must be straight. For plane wave incidence from an arbitrary direction, the first order contribution from each vertex to the far zone scattered field is obtained.

Since diffraction is a local phenomena at high frequencies the results obtained for a finite wedge may be applied to much more complex bodies made up of simple shapes. The field scattered by a three-dimensional shape constructed from flat plates may be approximated to first order as the sum of the contributions from each individual corner. The first order solution should be reasonably accurate in or near the specular regions as long as the object is convex. A convex body is defined here as a closed surface made up of flat plates such that all of the exterior wedge angles, taken between faces and exterior to the surface, are greater than 180 degrees. A simple example of an object that does not meet this requirement is a corner reflector. In this case, the effect of the interaction between the faces must be taken into account. Higher order effects such as double diffraction [7] and edge waves [8] are not considered in this chapter.

Note that the results presented in this paper are for a parallel ray type solution, that is, for a radar cross section result. The NEC - Basic Scattering Code (NEC-BSC)[9] is a near zone formulated code, that is it has a finite range involved. The UTD solutions are slightly different for this non-parallel ray case. The capabilities of the NEC-BSC and a comparable far zone code called the RCS-BSC are discussed in Reference [10].

## 2.2 Theoretical Background

There are many approximate solutions to the scattered field from a finite perfectly conducting wedge. Physical Optics and its extension the Physical Theory of Diffraction [11] is surface and edge current based. Geometrical Optics (GO) and its extensions the Geometrical Theory of Diffraction

(GTD) [12] and the Uniform Geometrical Theory of Diffraction [13] are ray based. The Method of Equivalent Currents (MEC) [14] is an intermediate type solution that was developed to handle caustic regions in the GTD. This has been augmented with the concept of stripping to provide better answers for flat plate problems [3]. Recently, Michaeli [15] showed a more rigorous approach in deriving equivalent currents. This was shown to be related to the incremental length method of Mitzner [16] by Knott [17]. These equivalent currents still had singularity problems that have been remedied by Michaeli [4] using a skewed coordinate system. Ufimtsev also derived a similar solution [18,19].

The above solutions can be cast in a corner diffraction coefficient form. These UTD ray type solutions have the advantage of being efficient for far zone flat plate problems since only the fields scattered from the corners need to be added. It also has the advantage that the results correlate to the scattering centers seen in high resolution measurements. Just the corner diffraction coefficient forms are outlined in this section.

A previous diffraction coefficient for a corner formed by the intersection of two straight edges was derived by Burnside and Pathak [3]. It is based on the asymptotic evaluation of the radiation integral containing the equivalent currents of Ryan and Peters [14]. The result was then empirically modified so that the diffraction coefficient would not change sign abruptly as it passes through the false shadow boundaries. It was derived for spherical wave incidence and remains valid for cases when the diffraction point is near the corner since the integral was evaluated for a saddle point near an end point; however, only the far zone result is shown here. The corner diffracted field due to one corner and one edge in the case of plane wave incidence and a far zone receiver is given by

$$\begin{bmatrix} E_{\beta_o}^c \\ E_{\phi}^c \end{bmatrix} = - \begin{bmatrix} E_{\beta_o}^i(Q_c) D_s^c(\phi, \phi', \beta_o, \beta_{oc}) \\ E_{\phi'}^i(Q_c) D_h^c(\phi, \phi', \beta_o, \beta_{oc}) \end{bmatrix} \frac{e^{-jks}}{s} \quad (2.1)$$

$$\begin{bmatrix} D_s^c \\ D_h^c \end{bmatrix} = \mp \begin{bmatrix} C_s(Q_e) \\ C_h(Q_e) \end{bmatrix} \frac{\sqrt{\sin \beta_o \sin \beta_{oc}}}{(\cos \beta_{oc} + \cos \beta_o)} \frac{e^{-j\frac{\pi}{4}}}{\sqrt{2\pi k}} \quad (2.2)$$

$$C_{s,h}(Q_e) = \frac{-e^{-j\frac{\pi}{4}}}{2n\sqrt{2\pi k} \sin \beta_a} \{ [D_o^c(\phi - \phi') + D_n^c(\phi - \phi')] \mp [D_o^c(\phi + \phi') + D_n^c(\phi + \phi')] \} \quad (2.3)$$



The new far zone corner diffraction solution is based on the PTD and cast into the form of the MEC and then into a UTD diffraction coefficient. This is done as follows. The PO is first used to approximate the currents resulting in a double integral over the surface. Stokes theorem is then applied to reduce the equation to a line integral [20,21]. The Michaeli currents are added to produce a total first order MEC result. This integral is then evaluated using the method of stationary phase to obtain the contribution from each corner [22].

The new corner diffraction coefficients are given in a form similar to previous expressions for diffraction coefficients:

$$\begin{bmatrix} E_{\beta}^c \\ E_{\phi}^c \end{bmatrix} = \begin{bmatrix} D_{\beta}^c & D_{\beta}^c \\ 0 & D_h^c \end{bmatrix} \begin{bmatrix} E_{\beta'}^i \\ E_{\phi'}^i \end{bmatrix} \frac{e^{-jk_s}}{s} \quad (2.9)$$

$$D_{s,h,2}^c = \pm \frac{j}{4\pi k} \left( \frac{1}{\cos \beta - \cos \beta'} \right) [d_{s,h,2}^{LPO} + d_{s,h,2}^{UTD} - d_{s,h,2}^{PO}] \quad (2.10)$$

where the plus or minus sign is chosen depending on which endpoint contribution is being calculated. The minus sign is used for the corner contribution associated with the negative t-axis, while the plus sign is used for the corner contribution associated with the positive t-axis. The edge fixed coordinates shown in Figure 2.2 are chosen such that  $\hat{n}$  is the outward normal of the O-face,  $\hat{t}$  is tangent to the edge, the positive b-axis lies on the O-face, and  $\hat{t} = \hat{b} \times \hat{n}$ . The expressions for  $d_{s,h,2}^{LPO}$ ,  $d_{s,h,2}^{UTD}$ , and  $d_{s,h,2}^{PO}$  are given by (O-face contribution only)

$$\begin{aligned} d_{s,h,2}^{LPO} &= \frac{1}{2} U^i c_{s,h,2}(\gamma, \phi') \left\{ \left[ \cot \left( \frac{\pi - (\gamma - \phi')}{4} \right) - \cot \left( \frac{\pi + (\gamma - \phi')}{4} \right) \right] \right. \\ &\quad \mp \left. \left[ \cot \left( \frac{\pi - (\gamma + \phi')}{4} \right) - \cot \left( \frac{\pi + (\gamma + \phi')}{4} \right) \right] \right\} \quad (2.11) \end{aligned}$$

$$\begin{aligned} d_{s,h,2}^{UTD} &= \frac{1}{n} c_{s,h,2}(\alpha, \pi - \alpha) \left[ \cot \left( \frac{\pi - (\alpha - \phi')}{2n} \right) \right. \\ &\quad \mp \left. \cot \left( \frac{\pi - (\alpha + \phi')}{2n} \right) \right] \quad (2.12) \end{aligned}$$

$$d_{s,h,2}^{PO} = \frac{1}{2} U^i c_{s,h,2}(\alpha, \phi') \left\{ \left[ \cot \left( \frac{\pi - (\alpha - \phi')}{4} \right) - \cot \left( \frac{\pi + (\alpha - \phi')}{4} \right) \right] \right\}$$

$$\mp \left[ \cot \left( \frac{\pi - (\alpha + \phi')}{4} \right) - \cot \left( \frac{\pi + (\alpha + \phi')}{4} \right) \right] \quad (2.13)$$

$$c_s(\delta, \epsilon) = -\frac{\sin \beta}{\sin \beta'} \quad (2.14)$$

$$c_h(\delta, \epsilon) = \frac{\sin \phi}{\sin \delta} \quad (2.15)$$

$$c_2(\delta, \epsilon) = -\frac{\sin \beta}{\sin \delta} (\cot \beta \cos \phi + \cot \beta' \cos \epsilon) \quad (2.16)$$

$$\cos \gamma = \frac{\sin \beta \cos \phi}{\sin \beta'} + \frac{(\cos \beta - \cos \beta')^2}{\sin \beta' (\sin \beta \cos \phi + \sin \beta' \cos \phi')} \quad (2.17)$$

$$\cos \alpha = \frac{\sin \beta \cos \phi}{\sin \beta'} + \frac{(\cos \beta - \cos \beta') \cos \beta'}{\sin^2 \beta'} \quad (2.18)$$

$$\cos^{-1} \mu = -j \ln \left( \mu + \sqrt{\mu^2 - 1} \right) \quad (2.19)$$

$$\sqrt{\mu^2 - 1} = \begin{cases} -|\sqrt{\mu^2 - 1}| & \mu < -1 \\ j|\sqrt{1 - \mu^2}| & -1 \leq \mu \leq 1 \\ |\sqrt{\mu^2 - 1}| & \mu > 1 \end{cases} \quad (2.20)$$

$$U^i = \begin{cases} 0 & , \pi - \phi' < 0 \\ 1 & , \pi - \phi' > 0 \end{cases} \quad (2.21)$$

where the + sign is associated with  $d_h^{LPO}$ ,  $d_2^{LPO}$ ,  $d_h^{UTD}$ ,  $d_2^{UTD}$ ,  $d_h^{PO}$ , and  $d_2^{PO}$  while the - sign is associated with the  $d_s^{LPO}$ ,  $d_s^{UTD}$ , and  $d_s^{PO}$  terms. The angles are defined in Figure 2.2. Since only convex structures are considered here proper shadowing of the rays is fairly simple. The shadowing of the incident field is accounted for by  $\vec{E}_{\beta'}^i$  and  $\vec{E}_{\phi'}^i$ , which are the components of the GO incident field. The shadowing of the diffracted ray is more complicated. The contributions from the LPO and PO components,  $d_{h,s,2}^{LPO}$  and  $d_{h,s,2}^{PO}$ , are present everywhere. The UTD components,  $d_{h,s,2}^{UTD}$ , are shadowed like diffracted fields. They do not contribute if the observation point is inside the wedge ( $\phi > n\pi$ ).

For the special case of a flat plate ( $n = 2$ ) the contribution from both faces may be found using

$$d_{h,2}^{LPO} = \frac{1}{2} S^i c_{s,h,2}(\gamma, \phi') \left\{ \left[ \cot \left( \frac{\pi - (\gamma - \phi')}{4} \right) - \cot \left( \frac{\pi + (\gamma - \phi')}{4} \right) \right] \right\}$$

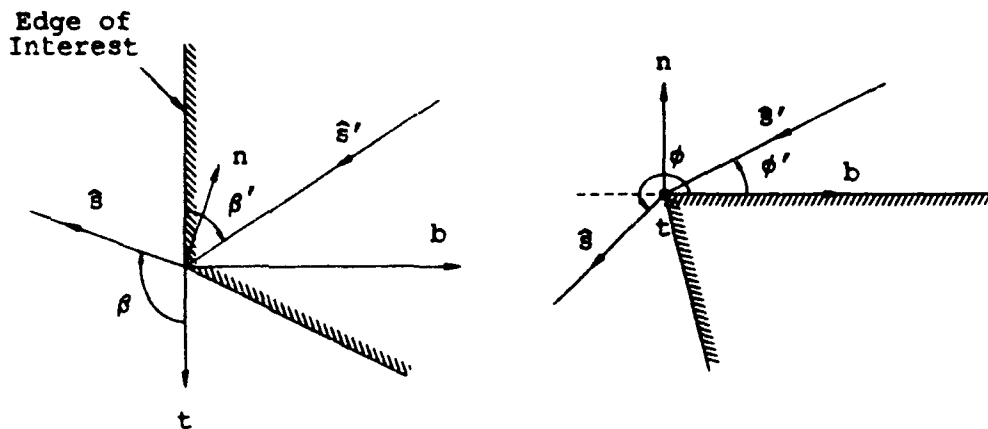


Figure 2.2: Definition of the Angles used in the New Corner Diffraction Coefficients.

$$\mp \left[ \cot \left( \frac{\pi - (\gamma + \phi')}{4} \right) - \cot \left( \frac{\pi + (\gamma + \phi')}{4} \right) \right] \quad (2.22)$$

$$d_{h,2}^{UTD} = \frac{1}{2} c_{h,2}^s(\alpha, \pi - \alpha) \left\{ \left[ \cot \left( \frac{\pi - (\alpha - \phi')}{4} \right) + \cot \left( \frac{\pi + (\alpha - \phi')}{4} \right) \right] \right. \\ \left. \mp \left[ \cot \left( \frac{\pi - (\alpha + \phi')}{4} \right) + \cot \left( \frac{\pi + (\alpha + \phi')}{4} \right) \right] \right\} \quad (2.23)$$

$$d_{h,2}^{PO} = \frac{1}{2} S^i c_{h,2}^s(\alpha, \phi') \left\{ \left[ \cot \left( \frac{\pi - (\alpha - \phi')}{4} \right) - \cot \left( \frac{\pi + (\alpha - \phi')}{4} \right) \right] \right. \\ \left. \mp \left[ \cot \left( \frac{\pi - (\alpha + \phi')}{4} \right) - \cot \left( \frac{\pi + (\alpha + \phi')}{4} \right) \right] \right\} \quad (2.24)$$

$$S^i = \begin{cases} -1 & , \pi - \phi' < 0 \\ 1 & , \pi - \phi' > 0 \end{cases} \quad (2.25)$$

where  $\gamma$ ,  $\alpha$ , and the other variables have been defined previously.

It is interesting to note that by writing the equations for the Michaeli equivalent currents and the new corner diffraction coefficients in cotangent form provide more insight into the connection of the new solutions with the previous methods. The new parameters separate out the optics currents and diffraction currents. This separation manifests itself in new parameters for

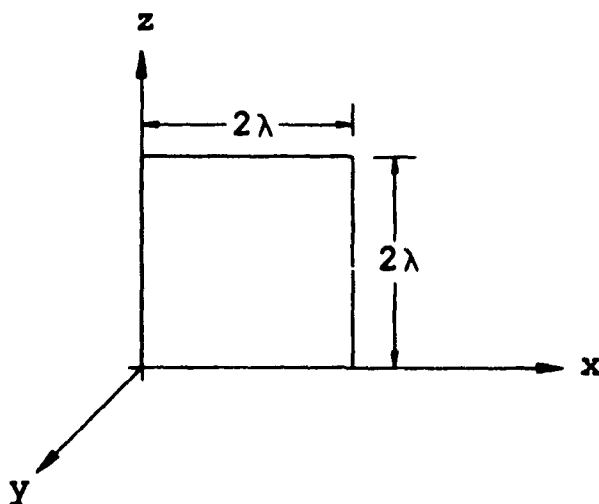


Figure 2.3: Two wavelength plate in the  $x$ - $z$  plane.

the  $\phi$  angles. They arise from the asymptotic evaluation of the currents in the skewed coordinate system chosen in physically meaningful directions. The LPO factor ( $\gamma$ ) is related to the projection of the average of the incident and diffraction planes on to the plane of the plate [1]. The PO and UTD factor ( $\alpha$ ) relates to the projection of the Keller diffraction cone on to the plane of the plate. It is easy to see in this form that in the Keller directions the LPO and PO cancel, leaving the UTD result formally used in many solutions.

## 2.3 Comparisons

The first example compares the Ryan and Peters equivalent currents, the previous and new corner diffraction solutions. The simple example of backscatter from a two wavelength square plate lying in the  $x$ - $z$  plane, as shown in Figure 2.3, is used. This illustrates that for backscatter these different methods produce very similar results, except for the very low level regions.

The co-polarized fields, in the principal plane, calculated using the three

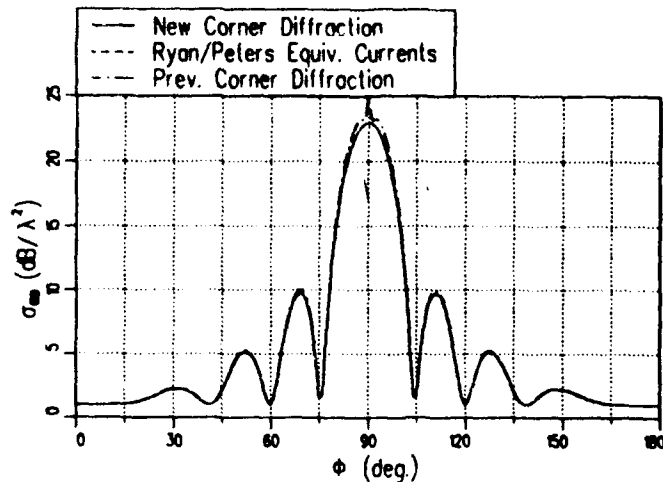


Figure 2.4: Backscatter from a 2 wavelength plate ( $\theta = 90^\circ$  pattern).

different methods are shown in Figures 2.4 and 2.5. All three methods give essentially the same results for the principal plane pattern cuts shown here. This is not surprising since the major contributions to the fields are the scattering from the two edges in their Keller cone directions. The new corner diffraction solution reduces to the Ryan and Peters equivalent current solution for points on the Keller cone [1], and the previous corner diffraction solution is essentially the same as Ryan and Peters equivalent current solution for most regions of space. The results in Figure 2.5 are for the horizontal ( $\sigma_{\phi\phi}$ ) polarization. For a knife edged plate such as this, the scattered field should be zero in the plane of the plate. Note that this is not the case in these first order results. The higher order terms (i.e. the double, triple etc. diffractions) produce the null for this polarization when they are included.

For patterns away from the principal plane, the higher levels are the same but the lower levels differ. This is illustrated by taking a conical cut ( $\theta = 60^\circ$ ) for the two wavelength plate. The results for the same three methods used previously are shown in Figures 2.6 and 2.7. In this case the methods agree well for the main lobe, however, they differ in the lower levels of the pattern.

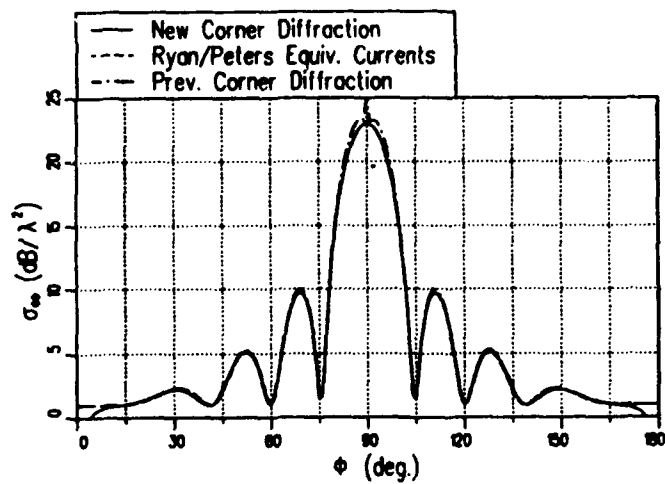


Figure 2.5: Backscatter from 2 wavelength plate ( $\theta = 90^\circ$  pattern).

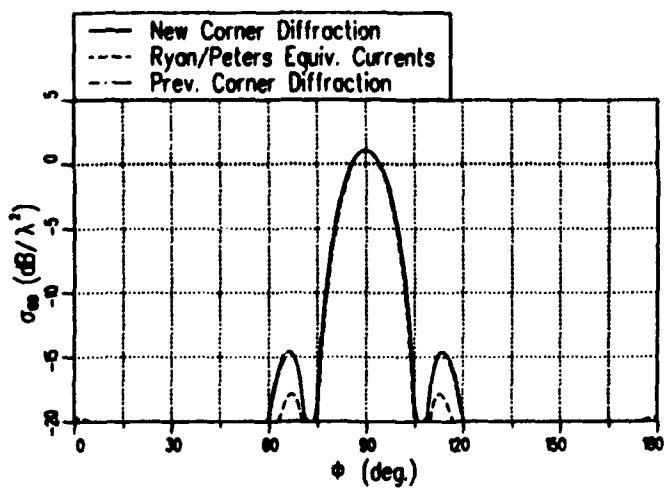


Figure 2.6: Backscatter from 2 wavelength plate ( $\theta = 60^\circ$  pattern).

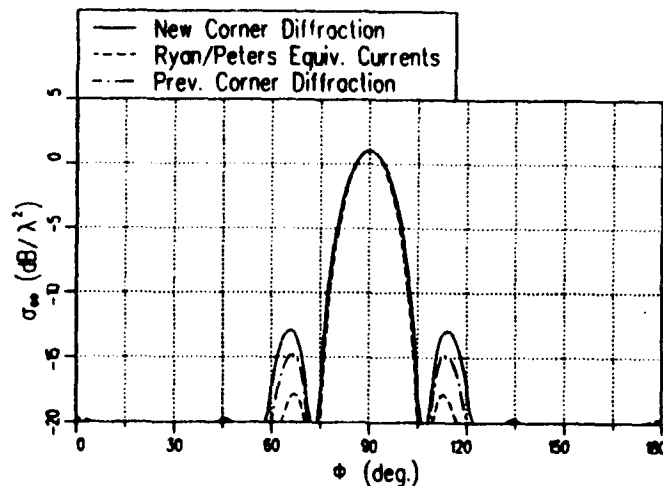


Figure 2.7: Backscatter from a 2 wavelength plate ( $\theta = 60^\circ$  pattern).

The differences in the three methods mentioned earlier are greatly increased for bistatic scattering problems. The bistatic scattering from a square plate two wavelengths on a side is examined to illustrate the point. The complete scattering matrix (all four values of  $\sigma$ ) is found for a plate in the x-y plane with a fixed source located at  $\theta^i = 45^\circ$  and  $\phi^i = 0^\circ$  as shown in Figure 2.8. The results for the  $\phi = 60^\circ$  pattern cut are compared with the previous corner diffraction solution and Method of Moment calculations for co-polarized fields in Figures 2.9 and 2.10. Similarly the results for the cross-polarized fields are given in Figure 2.11 and Figure 2.12. Overall the new solution agrees well with the Method of Moment calculations and does not exhibit the discontinuities which appear near  $\theta = 240^\circ$  and  $\theta = 300^\circ$  in the previous corner diffraction solution. The discontinuities in the previous corner diffraction solution are caused by the so called false shadow boundaries where the associated two-dimensional problem passes through a shadow boundary, but the three-dimensional problem in reality does not. The Ryan and Peters equivalent current results are not shown here, but they behave differently for similar reasons; that is, the solution still contains two dimension information in regions that it should not. In the region from  $\theta \approx 60^\circ$  to  $120^\circ$  (i.e. near the plane of the plate) the new solution and

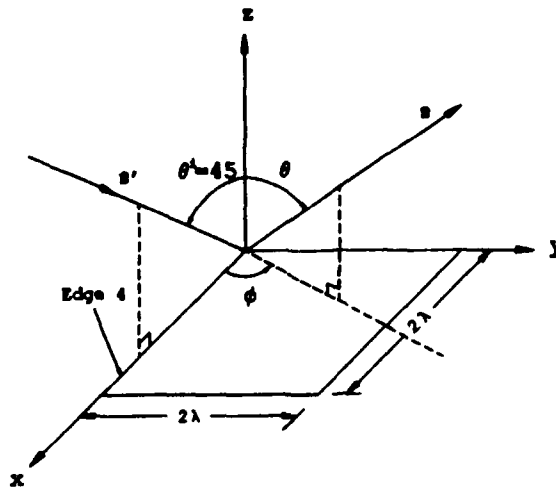


Figure 2.8:  $2\lambda$  square plate in the  $x$ - $y$  plane with a fixed source at  $\theta^i = 45^\circ$  and  $\phi^i = 0$ .

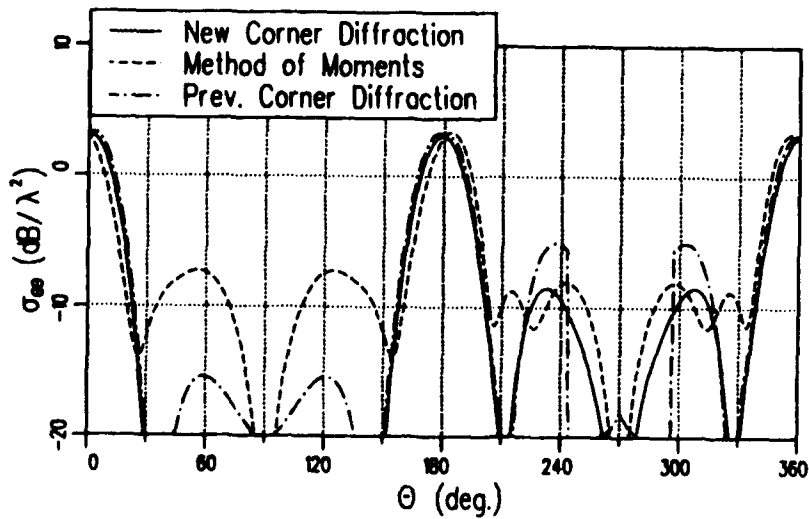


Figure 2.9: Co-polarized RCS in the  $\phi = 60^\circ$  plane of a  $2\lambda$  square plate with a  $\hat{\theta}^i$  polarized fixed source at  $\theta^i = 45^\circ$ ,  $\phi^i = 0^\circ$ .

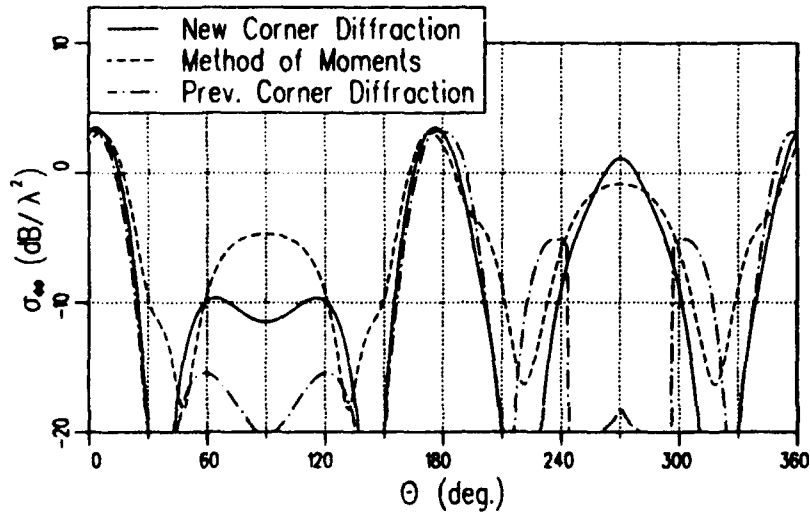


Figure 2.10: Co-polarized RCS in the  $\phi = 60^\circ$  plane of a  $2\lambda$  square plate with a  $\hat{\phi}^i$  polarized fixed source at  $\theta^i = 45^\circ$ ,  $\phi^i = 0^\circ$ .

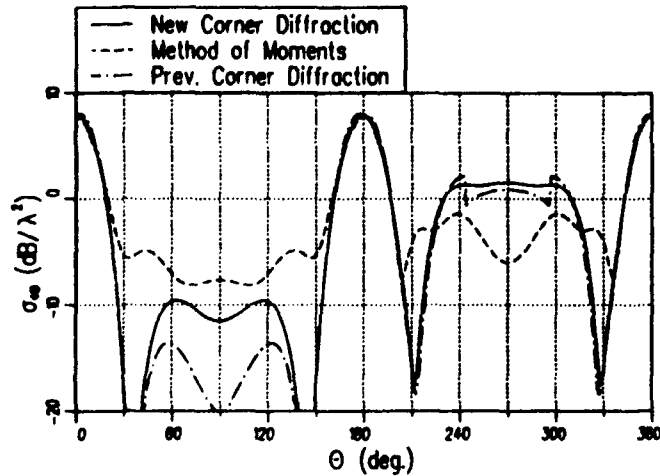


Figure 2.11: Cross-polarized RCS in the  $\phi = 60^\circ$  plane of a  $2\lambda$  square plate with a  $\hat{\theta}^i$  polarized fixed source at  $\theta^i = 45^\circ$ ,  $\phi^i = 0^\circ$ .

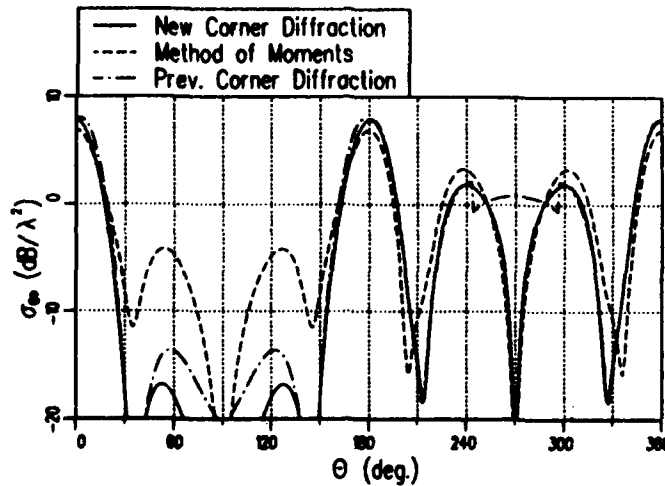


Figure 2.12: Cross-polarized RCS in the  $\phi = 60^\circ$  plane of a  $2\lambda$  square plate with a  $\hat{\phi}^i$  polarized fixed source at  $\theta^i = 45^\circ$ ,  $\phi^i = 0^\circ$ .

the Method of Moments solution differ by more than 20 dB. It is suspected that most of these differences are due to the effects of higher order terms (double and triple diffraction, edge waves) which are not included in the new solution.

In this example the new solution is compared to backscatter measurements [23] made at 10 GHz on a 6" cube. The geometry of the cube, tilted  $45^\circ$  in the  $x$ - $z$  plane, is illustrated in Figure 2.13. The results for the H-plane and E-plane patterns taken in the  $x$ - $y$  plane are given in Figures 2.14 and 2.15, respectively. The results agree well to first order over most regions of the pattern. The discrepancies are probably due to a combination of higher order terms not being included in the analysis and in measurements errors. The error in the measurements is likely two fold. First the faces of the cube model were misaligned slightly so they did not form edges as sharp as may be required. Secondly, it seems that there was some deviation from the desired pattern cuts as can be seen from the lack of symmetry in the measured patterns. In any case, they confirm the validity of the new corner diffraction solution within first order accuracy for wedge type structures.

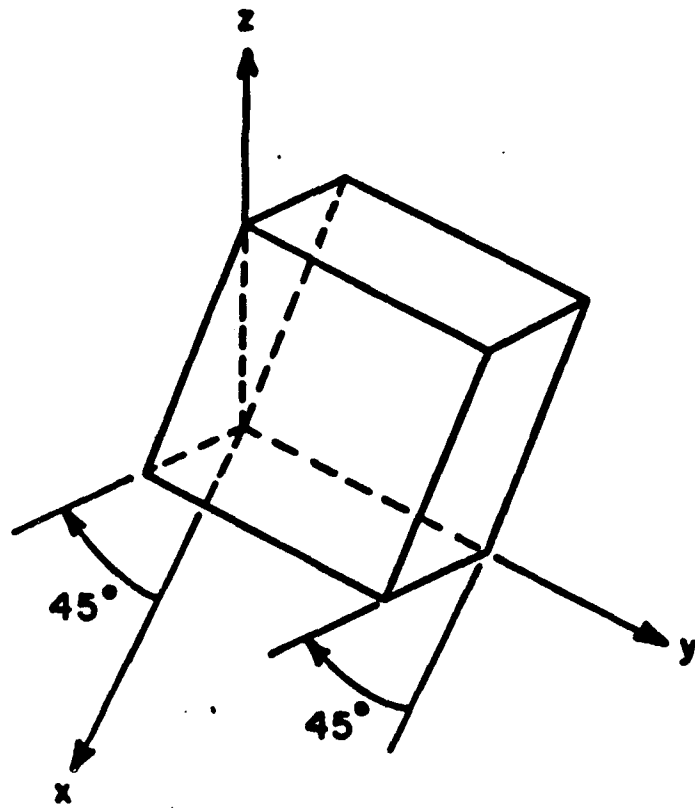


Figure 2.13: 6" Cube tilted 45° in the x-z plane.

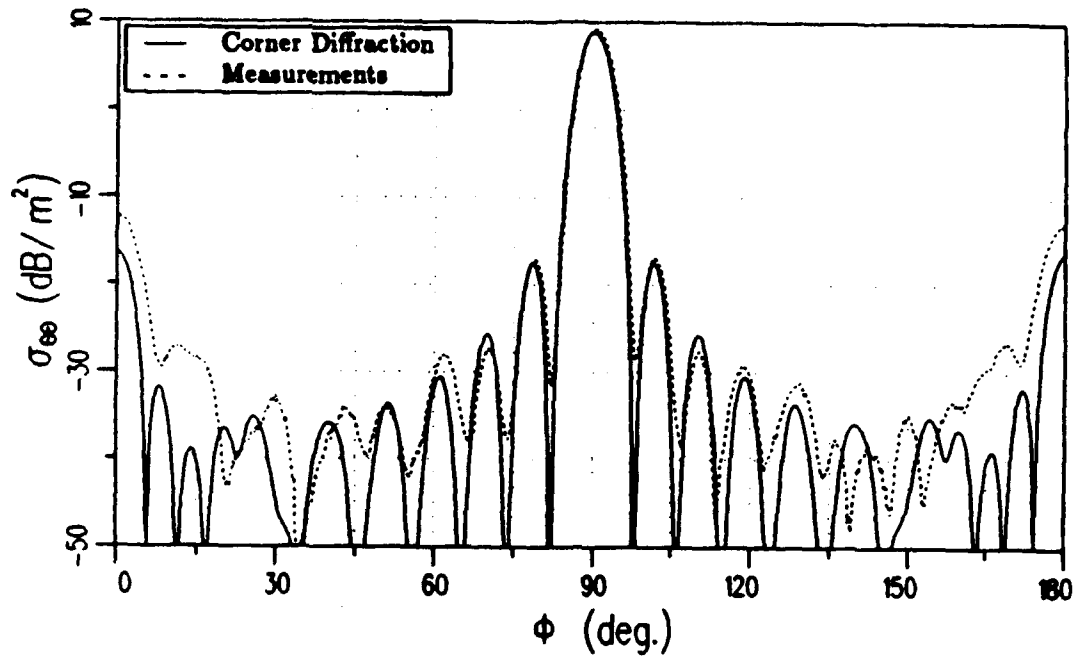


Figure 2.14: H-plane pattern for 6" cube tilted 45° in the x-z plane.

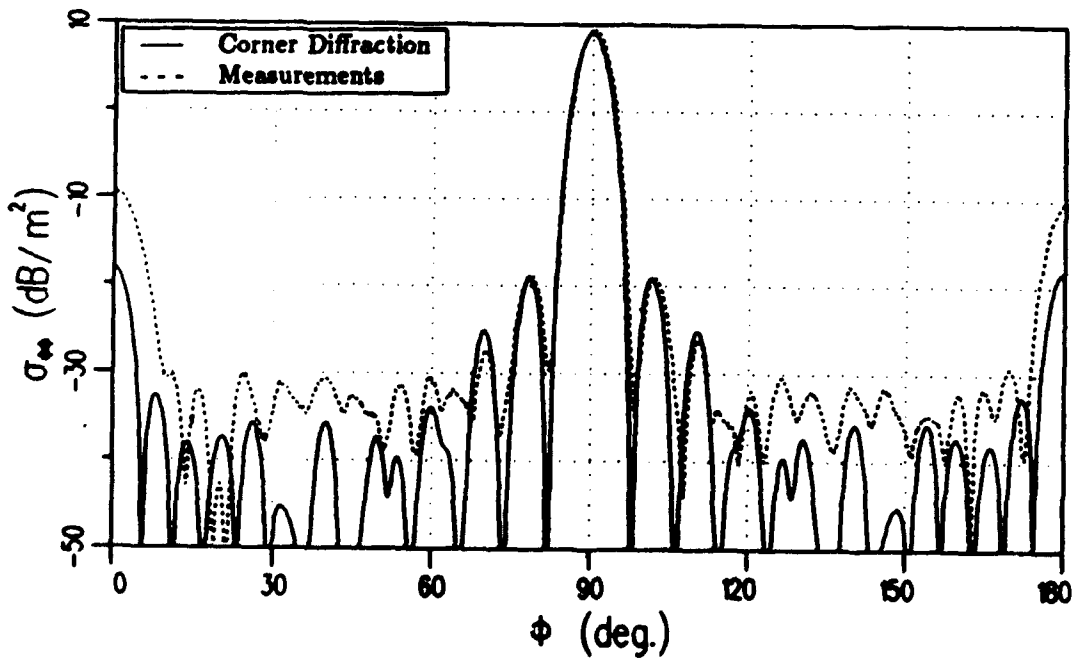


Figure 2.15: E-plane pattern for 6" cube tilted 45° in the x-z plane.

## 2.4 Discussion

The new corner diffraction coefficient in the above examples has been shown to provide improved results over other methods, especially in bistatic situations. The Michaeli equivalent currents have not been shown since they provide the same results as the new corner diffraction coefficient. Certain properties of these new solutions, however, may still cause patterns taken in some regions of space to be discontinuous.

It has been shown [4,1] that  $D_z^c$  and  $D_h^c$  do not tend to definite limits as  $\hat{s} \rightarrow \hat{\sigma}$  (i.e. the intersection of the associated half-plane and the Keller cone), where  $\hat{\sigma} = \hat{i} \sin \beta' + \hat{j} \cos \beta'$ , but they remain bounded. In practice, this means that both  $D_z^c$  and  $D_h^c$ , and therefore  $E_\beta^c$  and  $E_\phi^c$ , are discontinuous at this point in the pattern. A simple example illustrates how this discontinuity can affect a pattern. The bistatic RCS from the flat plate shown earlier in Figure 2.8 is considered. The source, linearly polarized in the  $\hat{\phi}^i$  direction, remains fixed at  $\theta^i = 45^\circ$  and  $\phi^i = 0^\circ$  while the pattern is taken near the x-y plane ( $\theta = 89^\circ$ ). The bistatic RCS is given in Figures 2.16 and 2.17 for the co-polarized and cross polarized fields, respectively. The abrupt null at  $\phi \approx 135^\circ$  in the co-polarized pattern and the spike at the same location in the cross-polarized pattern are due to discontinuities in the contribution from edge 4 (indicated in Figure 2.8). The point  $\phi \approx 135^\circ$  coincides with  $\beta_4 = \beta'_4$  and  $\phi_4 \approx 0$  where  $\beta_4$ ,  $\beta'_4$ , and  $\phi_4$  are the edge fixed coordinates for edge 4. Due to the geometry  $\hat{\beta}_4 \approx \hat{\phi}$  and  $\hat{\phi}_4 \approx \hat{\theta}$  so the discontinuity in  $\sigma_{\phi\phi}$  is due to the discontinuity in  $D_z^c$  and, likewise, the discontinuity in  $\sigma_{\theta\phi}$  is due to the discontinuity in  $D_h^c$ .

Therefore, the discontinuity in the new diffraction coefficients at the intersection of the Keller cone and the infinite half plane associated with the edge ( $\beta = \beta'$  and  $\phi = 0$ ) may be expected to cause discontinuities or narrow spikes depending on the polarization and the pattern cut. As the examples illustrate these disturbances only affect a typical pattern cut for around  $5^\circ$  to  $10^\circ$ . In addition, they are in the low level regions of the returns.

It is easily seen that the diffraction coefficients  $D_z^c$  and  $D_h^c$  are discontinuous as the source passes through the half plane  $\phi' = \pi$ . In the general case of bistatic scattering, these discontinuities in the sign of the field scattered by a corner will result in discontinuities in the total scattered field. However, the diffraction coefficients are continuous here ( $\phi' = \pi$ ) for the

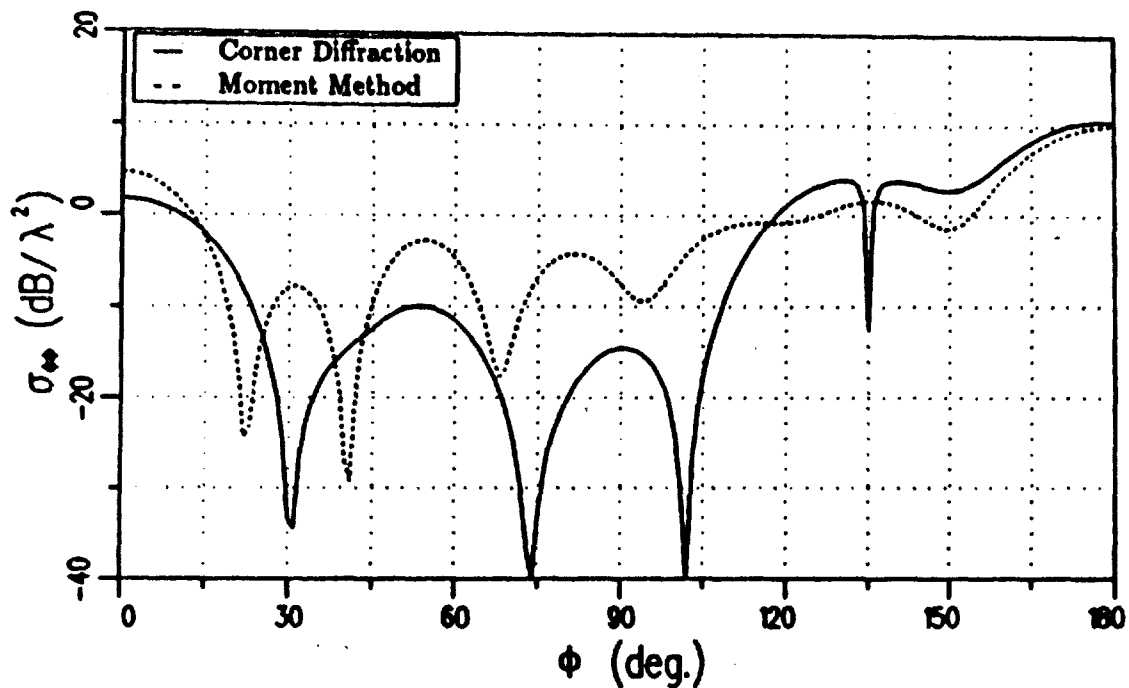


Figure 2.16: RCS for the  $\theta = 89^\circ$  cut of a  $2\lambda$  square plate with a  $\hat{\phi}^i$  polarized fixed source at  $\theta^i = 45^\circ$ ,  $\phi^i = 0^\circ$ .

special case of backscatter.

## 2.5 Conclusions

The objective of this paper has been to compare different methods for the analysis of the high frequency far zone scattering from flat plate and convex flat plate type structures. Ryan and Peters equivalent currents and the previous corner diffraction coefficient are compared with the Michaeli equivalent currents and the new corner diffraction coefficient. The method of moments and measurements are also used to validate the solutions.

It has been shown that for backscatter all the methods compare reasonably within engineering accuracy. For bistatic scattering, however, the two dimensional nature of the old methods lead to inaccuracies. The newer methods, based on more rigorous three dimensional analysis, remove most of these problems.

A new corner diffraction coefficient is presented that provides an efficient and accurate solution to within first order. It provides the same level of

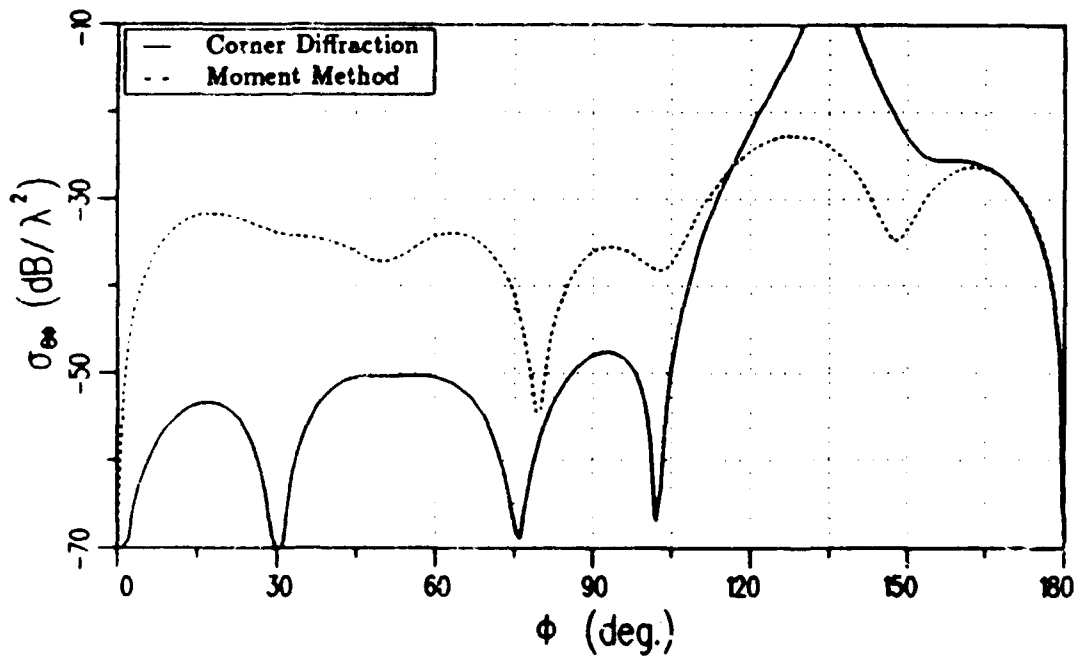


Figure 2.17: RCS for the  $\theta = 89^\circ$  cut of a  $2\lambda$  square plate with a  $\hat{\phi}^i$  polarized fixed source at  $\theta^i = 45^\circ$ ,  $\phi^i = 0^\circ$ .

accuracy as the Michaeli equivalent currents with the added benefit of not needing integrations for flat plates. All the optics and edge scattering effects have been lumped into the corners of the plate with nice physical interpretations.

## Chapter 3

# Edge Wave Vertex and Edge Diffraction

### 3.1 Introduction

The diffraction of acoustical waves by the tip of an elliptical perfectly conducting cone was studied by [24]. Satterwhite and Kouyoumjian [25] examined the vector electromagnetic problem and presented a Green's dyadic for a source radiating in the presence of an angular sector. However, their solution, expressed in terms of non-closed form Lamé functions, is cumbersome for numerical calculations. Furthermore, it has not so far appeared possible to asymptotically identify a "corner diffraction coefficient" from this eigenfunction representation.

Recently, Burnside and Pathak [26] proposed a corner diffraction coefficient which successfully predicts the corner effect of numerous plate structures. Their solution is based on the asymptotic evaluation of the radiation integral involving the equivalent currents that would exist in the absence of the corner. A corner diffraction term is then established by empirically modifying the final result. Sikta [8] applied a limiting process to the coefficient presented in [26] to derive the wave diffracted by the corner and propagating along one of the edges of a plane right angular sector. By introducing an empirically established "reflection coefficient" he utilized his edge wave corner diffraction coefficient in the calculation of double and triple diffraction by two adjacent corners of a flat plate structure.

The vertex and edge diffraction of an electromagnetic wave guided along

one of the edges of a semi-infinite wedge is studied asymptotically. A dipole source radiates in the close vicinity of the edge and excites a paraxial field guided by one of the edges of the trihedron - hence the term "edge wave". Explicit expressions of this field are given in Section 3.2 based on the limiting behavior of the Green's dyadic for an infinite wedge [27] as the dipole approaches its edge.

A first approximation of the vertex diffracted field is presented in Section 3.3, based on the radiation of the surface current that would be induced by the edge guided wave for an infinite wedge, which is subsequently truncated. The asymptotic evaluation of the surface current's radiation integral appropriately encounters the edge wave singularity consistent with Meixner's edge condition [28]. To the field expressions thus derived, a fringe current effect, which is asymptotically incorporated in the radiation integral of Michaeli's fringe edge equivalent currents [15,4,29], is superimposed. Edge wave vertex and edge diffraction coefficients can then be established from the asymptotic field expressions. The pertinent analysis is developed in Section 3.4.

The validity of the approach is confirmed via comparison with moment method results and pattern measurements for a small dipole radiating in the close vicinity of one of the edges of a polygonal plate.

## 3.2 Edge Waves

The term "edge waves" in the present work defines waves propagating along the edge of a wedge. The edge wave is actually a form of a maxwellian field guided by the edge, and exhibiting the proper edge singularity. Such a paraxial singular field can be excited either by a plane wave at grazing incidence, or by a dipole radiating in the close vicinity of the edge. The vertex of a terminated edge illuminated by a plane or spherical wave can also excite an edge wave. Independent of the excitation, but sufficiently far from its source, the edge wave behaves and can be treated as a ray optical field. However, application of ray optical techniques (UTD, UAT) is not straightforward, mainly due to the singular behavior of the paraxial fields.

Let us consider the more general problem of a point source  $\vec{j}^e = \vec{p}^e \delta(\vec{r} - \vec{r}')$  radiating in the presence of a perfectly conducting infinite wedge. The field produced by this dipole-wedge configuration can be formally written

$$\vec{E}(\vec{r}) = j\omega_0\mu_0\vec{\Gamma}(\vec{r}, \vec{r}') \cdot \vec{p}^e, \quad (3.1)$$

where  $\vec{\Gamma}(\vec{r}, \vec{r}')$  is the Green's dyadic for the wedge.

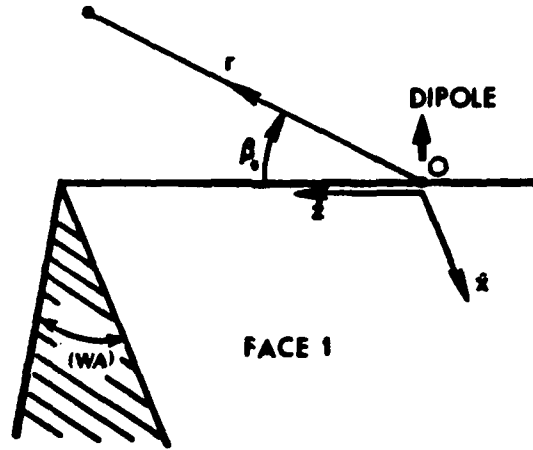


Figure 3.1: Dipole radiating in the close vicinity of the edge of a perfectly conducting wedge.

For convenience, the source point is located at  $S(\rho', \phi', 0)$ , ( $r' = \rho', \beta' = \pi/2$ ), in the system of coordinates with the  $z$ -axis being coincident with the edge and the  $x$ -axis parallel to face 1 of the wedge. The pertinent system of spherical coordinates is then  $(r, \beta_0, \phi)$  (Fig. 3.1). Furthermore, let  $kr \gg 1$ , so that the spherical Hankel functions of the second kind involved in the series representation assume their asymptotic form. The limiting form of the field in Equation 3.1 for small values of the parameter  $\epsilon = k\rho' \sin \beta_0$  is of interest here. After some straightforward manipulation it can be shown that

$$\vec{E}(\vec{r}) = j\omega_0\mu_0 C(\nu) (k\rho' \sin \beta_0)^{\nu-1} (\hat{\beta}_0 \cos \beta_0 \sin \nu\phi + \hat{\phi} \cos \nu\phi) \\ (p_{\rho'}^e \sin \nu\phi' + p_{\phi'}^e \cos \nu\phi') \frac{\exp(-jkr)}{r} + \vec{O}(\epsilon^0), \quad (3.2)$$

where  $\vec{O}(\epsilon^0)$  denotes the zero order remainder in the power series expansion

of the field. The constant factor  $C(\nu)$  is explicitly defined by

$$C(\nu) = \frac{\nu \Gamma(2\nu + 2) \exp\{j(\nu + 1)\pi/2\}}{\sqrt{\pi} 2^{3\nu+1} \Gamma(\nu) \Gamma(\nu + 1) \Gamma(\nu + 3/2)} \quad (3.3)$$

and

$$\nu = \frac{1}{n}, \quad n = \frac{2\pi - (WA)}{\pi}, \quad (3.4)$$

while (WA) is the wedge angle. In the case of the half plane ( $\nu = 1/2$ ), Equation 3.2 reduces to the following expression:

$$\vec{E}(\vec{r}) = -\frac{\sqrt{k} Z_0 \exp(j\pi/4)}{2\pi \sqrt{2\pi}} A^e(\rho', \phi') \frac{\hat{\beta}_0 \cos \beta_0 \sin(\phi/2) + \hat{\phi} \cos(\phi/2)}{\sqrt{\sin \beta_0}} \frac{\exp(-jkr)}{r} + \vec{O}(\epsilon^0), \quad (3.5)$$

where

$$A^e(\rho', \phi') = \frac{p_{\rho'}^e \sin(\phi'/2) + p_{\phi'}^e \cos(\phi'/2)}{\sqrt{\rho'}} \quad (3.6)$$

is a constant source factor.

The leading term in the power series expansion of the field (the edge wave), which will be denoted as  $\vec{E}^{ew}$  in the subsequent analysis, dominates in the paraxial region and reveals the strong coupling between the dipole source and the edge. It is a spherical ray optical wave that satisfies Maxwell's equations, the boundary conditions on the perfectly conducting surface, as well as Meixner's edge condition. The remainder  $\vec{O}(\epsilon^0)$  can be expressed in a closed form only for the case of the half plane and far field observations. Specifically, it can be obtained via reciprocity from the Fresnel integral (Sommerfeld) representation of the half plane canonical solution after subtracting the edge wave term. In the case of a general wedge angle, the remainder is essentially a power series of the small parameter  $\epsilon$ , the coefficients of which can be derived from the eigenfunction series representation of the Green's dyadic.

### 3.3 The Radiation Integral of the Edge Wave Currents in a Truncated Wedge

Clearly, the analysis of the waves associated with an infinite wedge does not include the effects of finite or semi-infinite edges. First, the edge wave term should be suitably modified so that the singularity, which results from the infinite edge, is eliminated. Second, the vertex and the terminating edges effects should be incorporated in the total solution. Asymptotically, the end point effect is additively introduced into the total solution and corresponds to a tip diffracted ray. On the other hand, the edge wave singularity is compensated multiplicatively with the introduction of a proper transition factor. Within this context, for a dipole radiating in the close vicinity of a terminated edge and sufficiently far from the vertex, the total field can be written as

$$\vec{E}^t \approx E^{\vec{e}w} \cdot \bar{T} + \vec{E}_1^e + \vec{E}_2^e + \vec{E}^c, \quad (3.7)$$

where  $\bar{T}$  is a transition dyadic to be determined,  $E_{1,2}^e$  are the edge diffracted edge waves associated with the two terminating edges, and  $\vec{E}^c$  is the vertex diffracted edge wave.

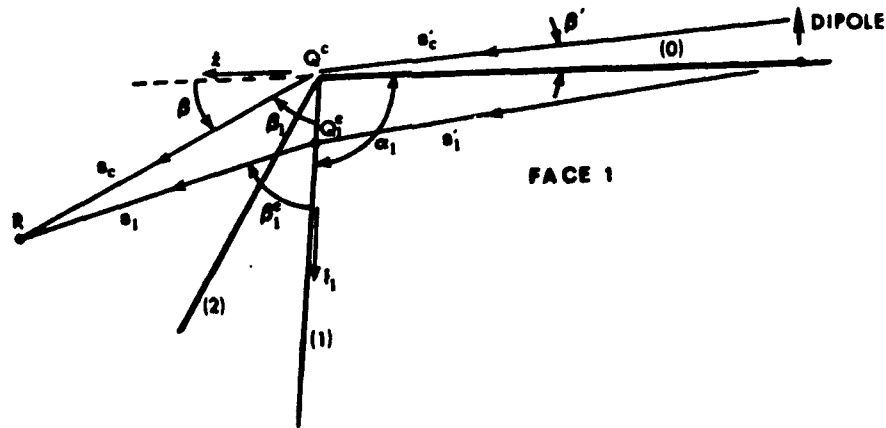


Figure 3.2: Geometry for the edge wave edge and vertex diffraction problem.

An approximation of the diffracted fields and an empirical determination

of the dyadic  $\overline{\overline{T}}$  is now developed. The excitation dipole is located in the close vicinity of the semi-infinite edge and sufficiently far from its vertex, as depicted in Fig. 3.2. For convenience, our attention is restricted to the diffracted fields associated with face 1 of the wedge. The results for face 2 can be readily derived by means of a simple transformation. Let  $\vec{j}_1(\vec{r}')$  be the total surface current flowing over the plane of face 1. The field associated with this current can be evaluated via the radiation integral in the Fresnel or Fraunhofer region of the surface, namely

$$\vec{E}_1(\vec{s}_c) = jkZ_0 \int \int_{S_1} \hat{R} \times \hat{R} \times \vec{j}_1(\vec{r}') \frac{\exp(-jkR)}{4\pi R} ds', \quad (3.8)$$

where  $\vec{s}_c$  and  $\vec{r}'$  is the vector from  $Q^c$  pointing to the observation point and the elementary surface patch  $ds'$ ,  $\hat{R} = (\vec{s}_c - \vec{r}')/R$ ,  $R = \|\vec{s}_c - \vec{r}'\|$ . The integration takes place over the truncated face of the wedge. It is assumed that  $\vec{j}_1(\vec{r}')$  can be adequately approximated by the actual induced currents as if the wedge was infinite, namely

$$\vec{j}_1(\vec{r}') \approx \hat{n}_1 \times \vec{H}^{ew}(\vec{r}') \Big|_{S_1}, \quad (3.9)$$

where  $\vec{H}^{ew}(\vec{r}')$  is the magnetic field produced by the dipole radiating in the close vicinity of the edge of an infinite wedge and  $\hat{n}_1$  is the unit vector normal to face 1. One may introduce the oblique system of coordinates  $(u, t_1)$  associated with the terminating edge (edge (1) in Fig. 3.2) and defined by the unit vectors

$$\hat{u} = \hat{z}, \quad \hat{t}_1 = \hat{x} \sin \alpha_1 - \hat{z} \cos \alpha_1,$$

with  $\alpha_1$  denoting the angle formed by the guiding edge and the terminating edge (edge (1)). Then, sufficiently far from the dipole, and employing the results of Section 3.2 one observes that

$$\vec{j}_1(u, t_1) \approx jk^\nu C(\nu) A_\nu^e(\rho', \phi') \sin^{\nu-1} \theta_0 \frac{\exp(-jkr_0)}{r_0} (\hat{x} \sin \theta_0 + \hat{z} \cos \theta_0), \quad (3.10)$$

in which

$$r_0 = \sqrt{t_1^2 \sin^2 \alpha_1 + (u - t_1 \cos \alpha_1 + s'_c)^2},$$

$$\sin \theta_0 = t_1 \sin \alpha_1 / r_0, \quad \cos \theta_0 = (u - t_1 \cos \alpha_1 + s'_c) / r_0,$$

$$A_\nu^c(\rho', \phi') = (\rho')^{\nu-1} (p_{\rho'}^c \sin \nu \phi' + p_{\phi'}^c \cos \nu \phi'),$$

$s'_c$  is the distance of the dipole source from the vertex, and the constant  $C(\nu)$  is defined by Equation 3.3. Based on the approximation in Equation 3.10 for the current, the vertex diffracted field associated with face 1 of the wedge and, essentially, representing the end point contribution to the radiation integral in Equation 3.8, can be expressed as follows:

$$\begin{aligned} \vec{E}_1^{c,po}(\vec{s}_c) \approx & \frac{jk^\nu Z_0 \sin^\nu \alpha_1 C(\nu) A_\nu^c(\rho', \phi') F(2kL_c \sin^2 \frac{\beta}{2})}{4\pi s_c (s'_c)^{\nu+1} (1 - \cos \beta)} \left\{ [s'_c \sin \beta I_{-\nu}^0(k) \right. \\ & - (\sin \beta \cos \alpha_1 + \sin \alpha_1 \cos \beta \cos \phi) I_{-\nu-1}^0(k)] \hat{\beta} \\ & \left. + \sin \alpha_1 \sin \phi I_{-\nu-1}^0(k) \hat{\phi} \right\}. \end{aligned} \quad (3.11)$$

In the above equation,  $I_{-p}^0(k)$  expresses the end point contribution to the integral

$$I_{-p}^0(k) = \int_0^\infty t^{p-1} \exp\{-jk(R + r_0)|_{u=0}\} dt,$$

which is examined in detail in [2]. For the specific semi-infinite wedge geometry under consideration, the integral  $I_{-p}^0(k)$  can be approximated by:

$$\begin{aligned} I_{-p}^0(k) \approx & \Gamma(p) k^{-p} \exp(jp\pi/2) \exp\{-jk(s_c + s'_c)\} \\ & \frac{F_{-p}^c[ka_1^2(\vec{s}_c; s'_c)]}{[\sin \alpha_1 \sin \beta \cos \phi + \cos \alpha_1 (1 - \cos \beta)]^p}, \end{aligned} \quad (3.12)$$

in which

$$a_1(\vec{s}_c; s'_c) = -\text{sign}(\pi - \alpha_1 - \beta_1) \left| \sqrt{(s'_c + s_c) - (s'_1 + s_1)} \right| \quad (3.13)$$

and  $s'_1, s_1$  denote the distance of the dipole source point and the receiver from the origin  $Q_1^c$  of the Keller cone of diffracted rays from the terminating edge (edge (1) in Fig. 3.2). The branch of the bracketed expression in the denominator of Equation 3.12 is chosen according to

$$(-1)^p = \exp(jp\pi).$$

The factor  $F(\cdot)$  is the familiar edge transition function of UTD [13], while the edge wave transition function  $F_{-p}^c(|\cdot|)$  is defined by

$$F_{-p}^c(x) = \exp(jp\pi/4) (2x)^{p/2} \exp(jx/2) \mathcal{D}_{-p}[\exp(j\pi/4)\sqrt{2x}], \quad (3.14)$$

with  $\mathcal{D}_{-p}(\cdot)$  denoting the parabolic cylinder function of order  $-p$  [30,31]. When  $x > 0$  is small

$$F_{-p}^c(x) \approx \sqrt{\pi} \exp(jp\pi/4) x^{p/2} \exp(jx/2) \cdot \left[ \frac{1}{\Gamma(\frac{p+1}{2})} - \frac{2 \exp(j\pi/4)}{\Gamma(\frac{p}{2})} \sqrt{x} + \frac{j(p-1/2)}{\Gamma(\frac{p+1}{2})} x + \dots \right] \quad (3.15)$$

and when  $x$  is large

$$F_{-p}^c(x) \approx 1 - \frac{p(p+1)}{4jx} - \frac{p(p+1)(p+2)(p+3)}{32x^2} + \dots \quad (3.16)$$

Retaining only the dominant term in the expression of the vertex diffracted wave (dominant with respect to the parameter  $2ks'_c$ ) and assuming the approximation [32]

$$s'_{1,2} + s_{1,2} \approx (s'_c + s_c) - L_c [1 + \cos(\alpha_{1,2} + \beta_{1,2})], \quad (3.17)$$

for large values of the distance parameter  $L_c = s_c s'_c / (s_c + s'_c)$ , one obtains the following expression for the vertex diffracted field, in terms of the edges (1) and (2) fixed coordinate systems:

$$\begin{aligned} \vec{E}^{c,p\phi}(\vec{s}_c) \approx & \frac{\exp(j\nu\pi/2) \Gamma(\nu) C(\nu)}{k} \frac{E_{\beta'}^i(Q^c) \sin \nu\phi' + E_{\phi'}^i(Q^c) \cos \nu\phi'}{\sin^{1-\nu} \beta'} \\ & \cdot \cot \frac{\beta}{2} F(2kL_c \sin^2 \frac{\beta}{2}) \left\{ \frac{\sin^\nu \alpha_1 F_{-\nu}^c[2kL_c \cos^2(\frac{\alpha_1 + \beta_1}{2})]}{(\cos \alpha_1 + \cos \beta_1)^\nu} \right. \\ & \left. + \frac{\sin^\nu \alpha_2 F_{-\nu}^c[2kL_c \cos^2(\frac{\alpha_2 + \beta_2}{2})]}{(\cos \alpha_2 + \cos \beta_2)^\nu} \right\} \frac{\exp(-jk s_c)}{s_c} \hat{\beta}. \quad (3.18) \end{aligned}$$

In Equation 3.18,  $E_{\beta',\phi'}^i(Q^c)$  represent the components of the free space dipole field at  $Q^c$  with respect to the guiding edge fixed coordinate system. We refer to the above term as the physical optics component of the vertex

diffracted field. As a matter of fact, the above UTD form of the vertex diffracted wave is derived from currents determined from the interaction of the dipole source and the guiding edge only. The effect of the terminating edges, clearly, has not been included yet. It should be, however, emphasized that this terminology should not imply any connection with the common Physical Optics approach, where the surface current is approximated with the superposition of the tangential component of the superimposed incident and reflected magnetic fields.

### 3.4 An Equivalent Current Approach

It can be easily shown that the surface radiation integral in Equation 3.8 can be asymptotically reduced to a line integral along the terminating edges of the semi-infinite structure. Thus, the high frequency approximation of the edge and vertex diffracted fields can be viewed as the stationary phase and end point contribution, respectively, of the radiation integral of equivalent line sources "excited" by the impinging edge wave. As far as the "physical optics" effect described in Section 3.3 is concerned, the same expression for the field, excluding the factor  $F[2kL_c \sin^2(\beta/2)]$ , can be obtained via the asymptotic approximation of the line radiation integral of the physical optics components of Michaeli's equivalent currents flowing along edges (1) and (2) and being proportional at each point to the tangential components of the incident edge wave. This observation suggests the addition of a fringe effect to the physical optics diffracted field which is, similarly, described by the radiation integral of Michaeli's fringe currents. Although the latter have been derived for plane wave incidence, reasonable results are obtained if one generalizes the same concepts for arbitrary (non-uniform) ray optical wavefronts and, hence, for an edge wave singular at the edge.

As before, our attention is restricted to face 1 of the wedge. The equivalent edge currents presented by Michaeli [15,4,29] for grazing edge wave incidence at the point  $Q_1$  of the edge (1) may be expressed in the form

$$I_1(Q_1) = \frac{2j}{k} \frac{\vec{H}^{ew}(Q_1) \cdot \hat{t}_1}{2} i_1(Q_1) \quad (3.19)$$

$$M_1(Q_1) = \frac{2jZ_0}{k} \frac{\vec{H}^{ew}(Q_1) \cdot \hat{t}_1}{2} m_1(Q_1), \quad (3.20)$$

$\hat{t}_1$  is the unit vector tangent to the edge at  $Q_1$  and  $i_1, m_1$  are known and, in general, slowly varying functions of the observer's location in the vertex fixed coordinate system and the distance of  $Q_1$  from the tip  $Q^c$  of the trihedron. A factor of  $1/2$  should be also introduced due to grazing incidence [13].

It is presumed that the edge and vertex diffracted edge wave associated with face 1 of the wedge can be approximated by the radiation integral of the equivalent currents  $I_1(Q_1), M_1(Q_1)$  flowing along the edge (1), which, in the Fresnel or the Fraunhofer region of the edge, can be explicitly written as

$$\begin{aligned} \vec{E}_1^d(\vec{s}_c) \approx & jk^\nu Z_0 \sin^\nu \alpha_1 C(\nu) A_\nu^c(\rho', \phi') s'_c \\ & \cdot \int_0^\infty [\hat{R} \times \hat{R} \times \hat{t}_1 i_1(\vec{s}_c; t_1) + \hat{R} \times \hat{t}_1 m_1(\vec{s}_c; t_1)] \\ & \cdot t_1^{\nu-1} \frac{\exp\{-jk(R+r_1)\}}{4\pi R r_1^{\nu+1}} dt_1, \end{aligned} \quad (3.21)$$

with  $R = \|\vec{s}_c - t_1 \hat{t}_1\|$  and  $\hat{R} = (\vec{s}_c - t_1 \hat{t}_1)/R$ .

### 3.4.1 Edge Wave Vertex Diffracted Field

The phase of the integrand in Equation 3.21 exhibits a stationary phase point in the neighborhood of an end point, the latter being coincident with the branch singularity of the integrand. Therefore, for large values of the parameter  $k$  the asymptotic evaluation of the integral reveals a vertex contribution as well as an edge diffracted term, if

$$\cos \alpha_1 (1 - \cos \beta) + \sin \alpha_1 \sin \beta \cos \phi > 0,$$

i.e., if  $Q_1^c$  lies on the edge (1) itself rather than on its extension. Without presenting the details of the asymptotic approximation, one obtains the approximate vertex diffracted field, associated with face 1 of the wedge

$$\begin{aligned} \vec{E}_1^c(\vec{s}_c) \approx & \exp\{j(\nu+1)\pi/2\} \Gamma(\nu) C(\nu) Z_0 A_\nu^c(\rho', \phi') \frac{\exp\{-jk(s_c + s'_c)\}}{4\pi s_c (s'_c)^\nu} \cdot \\ & \vec{G}_1^c(\vec{s}_c) \frac{F_{-\nu}^c[ka_1^2(\vec{s}_c; s'_c)]}{[\cot \alpha_1 (1 - \cos \beta) + \sin \beta \cos \phi]^\nu}, \end{aligned} \quad (3.22)$$

in which we have substituted

$$\vec{G}_1^c(\vec{s}_c) = \hat{s}_c \times \hat{s}_c \times \hat{t}_1 i_1(Q^c) + \hat{s}_c \times \hat{t}_1 r_{v_1}(Q^c) \quad (3.23)$$

The previous discussion also suggests the decomposition

$$\left\{ \begin{array}{l} i_1(Q^c) \\ m_1(Q^c) \end{array} \right\} = \left\{ \begin{array}{l} i_1^f(Q^c; \mu_1^f) \\ m_1^f(Q^c; \mu_1^f) \end{array} \right\} + \left\{ \begin{array}{l} i_1^{po}(Q^c; \mu_1^{po}) \\ m_1^{po}(Q^c; \mu_1^{po}) \end{array} \right\} \quad (3.24)$$

and  $i_1(Q^c)$ ,  $m_1(Q^c)$ ,  $i_1^{po,f}(Q^c; \mu_1^{po,f})$ ,  $m_1^{po,f}(Q^c; \mu_1^{po,f})$  can be obtained from [15,4,29] along with the definitions in Equations 3.19 and 3.20. The parameters  $\mu_1^{po,f}$  involved in the expressions of the edge equivalent currents depend on the choice of the edge fixed coordinate system and, in particular, on the angle between the tangent to the edge at  $Q_1$  and the unit vector  $\hat{\sigma}$  tangent to face 1 at  $Q_1$  which may be chosen arbitrarily. When the currents are truncated to reveal an end point effect, one should be cautious about the choice of the parameters  $\mu_1^{po,f}$ , i.e., the choice of the edge fixed coordinate system, so that the terminated equivalent edge currents represent correctly the end point effect of the truncated, by the edges of the trihedron, true surface induced currents. Within this context, a correct choice of the parameter  $\mu_1^{po}$  for the physical optics component of the equivalent currents is

$$\mu_1^{po} = \frac{\sin \alpha_1 \sin \beta_1 \cos \phi_1 + \cos \alpha_1 (\cos \beta_1 + \cos \alpha_1)}{\sin^2 \alpha_1}, \quad (3.25)$$

so that the unit vector  $\hat{\sigma}$  is parallel to the guiding edge, whereas for the fringe currents the proper choice is

$$\mu_1^f = \frac{\sin \alpha_1 \sin \beta_1 \cos \phi_1 - \cos \alpha_1 (\cos \beta_1 + \cos \alpha_1)}{\sin^2 \alpha_1} \quad (3.26)$$

and, now,  $\hat{\sigma}$  is parallel to the edge diffracted ray from  $Q^c$  that grazes the plane of face 1. Not surprisingly, using Equation 3.25 for the definition of the parameter  $\mu_1^{po}$  in the expressions of the physical optics equivalent edge currents one finds

$$\vec{G}_1^{c,po}(\vec{s}_c) = -\hat{\beta} \cot \frac{\beta}{2}, \quad (3.27)$$

so that the vertex diffracted field assumes the approximation

$$\vec{E}_1^c(\vec{s}_c) \approx \vec{E}_1^{c,po}(\vec{s}_c) + \vec{E}_1^{c,f}(\vec{s}_c) \quad (3.28)$$

in which  $\vec{E}_1^{c,p0}(\vec{s}_c)$  is identical with the term associated with face 1 in Equation 3.18, while the fringe currents related wave is equal to

$$\begin{aligned} \vec{E}_1^{c,f}(\vec{s}_c) \approx & \exp\{j(\nu + 1)\pi/2\} \Gamma(\nu) C(\nu) Z_0 A_L^c(\rho', \phi') \sin^\nu \alpha_1 \\ & \cdot \frac{\exp\{-jk(s_c + s'_c)\}}{4\pi s_c (s'_c)^\nu} F(2kL_c \sin^2 \frac{\beta}{2}) \\ & \cdot \frac{\vec{G}_1^{c,f}(\vec{s}_c) F_{-\nu}^c[ka_1^2(\vec{s}_c; s'_c)]}{(\cos \alpha_1 + \cos \beta_1)^\nu} \end{aligned} \quad (3.29)$$

The vector function  $\vec{G}_1^{c,f}(\vec{s}_c)$  is related with Michaeli's equivalent currents at  $Q^c$  via the equation

$$\vec{G}_1^{c,f}(\vec{s}_c) = i_1^f(Q_c; \mu_1^f) \hat{s}_c \times \hat{s}_c \times \hat{t}_1 + m_1^f(Q_c; \mu_1^f) \hat{s}_c \times \hat{t}_1 \quad (3.30)$$

The above expressions simplify considerably for the case of the plane angular sector, with  $\alpha_1 = \alpha_2 = \alpha$ ,  $a_1 = a_2 = a$ . Without presenting the details of the derivation, which involves only elementary manipulations, for the field related with the fringe currents one derives

$$\begin{aligned} \vec{E}^{c,f}(\vec{s}_c) \approx & \frac{-jZ_0}{\sqrt{2}\pi} A^c(\rho', \phi') \frac{\exp\{-jk(s_c + s'_c)\}}{4\pi s_c \sqrt{s'_c}} \\ & F(2kL_c \sin^2 \frac{\beta}{2}) \frac{\vec{G}^{c,f}(\vec{s}_c; \alpha) F_{-1/2}^c[ka^2(\vec{s}_c; s'_c)]}{\sqrt{\cot \alpha (1 - \cos \beta) + \sin \beta \cos \phi}}, \end{aligned} \quad (3.31)$$

where the function  $G^{c,f}(\vec{s}_c)$  is given by

$$\vec{G}^{c,f}(\vec{s}_c) = \frac{1}{\cos(2\alpha) + \cos \delta} \left[ -\hat{\beta} \sin \beta + \frac{\hat{\beta} e_\beta(\beta, \phi) + \hat{\phi} e_\phi(\beta, \phi)}{\sin^2 \alpha \sin \beta_1 \cos(\delta/2)} \right], \quad (3.32)$$

with

$$\cos \delta = \sin(2\alpha) \sin \beta \cos \phi - \cos(2\alpha) \cos \beta, \quad (3.33)$$

$$\begin{aligned} e_\beta(\beta, \phi) = & -(\cos \alpha + \cos \beta_1) (\sin \alpha \cos \beta \cos \phi + \cos \alpha \sin \beta) \\ & \cdot [\sin \alpha \cos \phi_1 (1 - \cos \alpha \cos \beta_1) - \cos^2 \alpha \sin \beta_1] \\ & + \sin^5 \alpha \sin \phi \sin \phi_1, \end{aligned} \quad (3.34)$$

$$e_\phi(\beta, \phi) = \sin \alpha \sin \phi (\cos \alpha + \cos \beta_1) \cdot [\sin \alpha \cos \phi_1 (1 - \cos \alpha \cos \beta_1) - \cos^2 \alpha \sin \beta_1] + \sin^4 \alpha \sin \phi_1 (\sin \alpha \cos \beta \cos \phi + \cos \alpha \sin \beta). \quad (3.35)$$

For the particular case of the right angle angular sector ( $\alpha = \pi/2$ ), it readily follows that

$$\vec{G}^{c,f}(\vec{s}_c; \pi/2) = \hat{\beta} (\cot \frac{\beta}{2} - \csc \frac{\beta}{2}) \quad (3.36)$$

and the total corner diffracted field assumes the simple representation

$$\vec{E}^c(\vec{s}_c) \approx \frac{-jZ_0}{\sqrt{2}\pi} A^c(\rho', \phi') \frac{\exp\{-jk(s_c + s'_c)\}}{4\pi s_c \sqrt{s'_c}} \cdot \frac{F(2kL_c \sin^2 \frac{\beta}{2})}{\sin \frac{\beta}{2}} \frac{F_{-1/2}^c[kL_c(1 - \sqrt{1 - \sin^2 \beta \cos^2 \phi})]}{\sqrt{\sin \beta \cos \phi}} \hat{\beta}, \quad (3.37)$$

where  $A^c(\rho', \phi')$  is defined by Equation 3.6.

### 3.4.2 Edge Wave Edge Diffracted Field

It can be shown that the edge diffracted field, i.e., the stationary phase contribution to the radiation integral of Michaeli's equivalent currents, is the edge diffracted edge wave predicted by UTD, multiplicatively corrected by the transition function

$$F_{\nu-1}^c[2kL_{e_1} \cos^2 \left( \frac{\alpha_1 + \beta_1}{2} \right)]$$

where

$$F_{\nu-1}^c(\cdot) = [F_{\nu-1}^c(\cdot)]^* \quad (3.38)$$

with the star denoting complex conjugate. The large parameter  $L_{e_1}$  equals

$$L_{e_1} = \frac{s_1 s'_1}{s_1 + s'_1} \quad (3.39)$$

The transition function  $F_{\nu-1}^c(\cdot)$  guarantees the finiteness of the edge diffracted edge wave as  $Q_1^c \rightarrow Q^c$  and the uniformity (continuity) of the total field

as the "shadow boundary" of the edge diffracted rays (the cone  $[\text{cct } \alpha_1(1 - \cos \beta) + \sin \beta \cos \phi] = 0$ ) is crossed. It appears as a type of caustic correction factor in the sense that it compensates the singularity of the edge diffracted field at the extension of the guiding edge. However, in our case the singularity arises from the behavior of the incident field on the edge rather than the focusing of the diffracted rays into a caustic.

### 3.4.3 A Heuristic Correction Factor for the Direct Edge Wave

As pointed out earlier, the rigorous solution of the radiation of a dipole in the presence of an infinite wedge predicts a singular field at the edge of the wedge, in consistency with Meixner's edge condition. However, this singularity of the edge wave is not physically acceptable when  $\beta \rightarrow 0$ . To overcome this discrepancy, the multiplicative correction of the edge wave associated with a semi-infinite or finite edge with the use of a suitable transition function (in general a dyadic) has been suggested. Such a transition function can be empirically derived by requiring the continuity of the total field at the shadow boundaries of the direct wave (edge wave), namely at the planes  $\phi_{1,2} = \pi$ . This continuity was guaranteed by the UTD evaluation of the edge diffracted field, but it is violated in the paraxial region after the introduction of the function  $F_{\nu-1}^e$ , which assures the uniformity of the total diffracted field. Obviously, the edge wave can be multiplied by a similar transition function so that the total field retains its continuity in the paraxial region as well as outside of it, where the transition function recedes to unity. In addition, such a multiplicative correction would yield a finite total field along the extension of the edge.

In particular, for the plane angular sector, a convenient modification of the edge wave, in the extension of the guiding edge, reads

$$\begin{aligned} \vec{E}^{ew}(\vec{s}_c) \approx & -\frac{\sqrt{k}Z_0 \exp(j\pi/4)}{2\pi\sqrt{2\pi}} A^e(\rho', \phi') \\ & \cdot [\hat{\beta}_0 \cos \beta_0 \sin(\phi/2) + \hat{\phi} \cos(\phi/2)] \\ & \frac{F_{-1/2}^e[2kL_e \sin^2 \beta_0]}{\sqrt{\sin \beta_0}} \exp(-jk s_0) \Big|_{s_0}, \end{aligned} \quad (3.40)$$

with  $s_0$  denoting the distance of the observation point from the dipole and

$\beta_0$  is the elevation angle of the observer in the guiding edge fixed coordinate system centered at the point of the projection of the dipole onto the edge.

### 3.5 Discussion and Numerical Results

The edge wave vertex diffracted field is a higher order term with respect to the large parameter  $k$  in the asymptotic solution of the radiation of a dipole in the vicinity of the edge of a trihedron. Nonetheless, it contributes significantly to the  $\hat{\beta}$ -directed component of the field, especially in the paraxial region of the guiding edge and along its extension. This is due to the accumulation of electric current flow lines in the vicinity of the guiding edge excited by the ray optical edge wave.

The solution, based on Michaeli's equivalent currents, is essentially an asymptotic PTD approach, in that a fringe current effect due to the terminating edges is added to the edge wave currents, cast into a UTD form. The rigorousness of the approach may be questioned at this point, since the derivation of the fringe edge currents assume an infinite edge and uniform plane wave illumination. However, the field is expected to retain its singular behavior in the vicinity of the vertex, which, moreover, does not contradict the "tip condition" (i.e., the behavior of the field in the neighborhood of a vertex) as investigated rigorously by several authors. It should be emphasized that the approximations attempted in Sections 3.3 and 3.4 by no means present a complete rigorous representation of the tip diffracted field, but it merely includes the information of the truncation of known components of the currents flowing over the wedge surface and can serve as a good engineering approximation to the problem. Again in a PTD context, the completeness of a solution requires the addition of a vertex current component, i.e., a current excited by the vertex of the trihedron, which however remains unknown.

The patterns of the *total diffracted* field predicted by the "Physical Optics" solution and the equivalent currents approximation, for the configuration shown in Fig. 3(a), are compared in Fig. 3.4. Clearly, the "physical optics" tip diffracted wave is not adequate to compensate the discontinuity of the edge wave edge diffracted field. On the other hand, the equivalent currents result yields a continuous pattern across the shadow boundary cone of the terminating edge diffracted rays, and appears as a more com-

plete representation of the diffraction effects.

Comparisons of the calculated field (which includes *only* the two edge wave tip diffracted terms corresponding to the two adjacent corners added to the modified direct edge wave) via Michaeli's equivalent currents (denoted as MEC on the graphs) and the "Physical Optics" approach (PO) with moment method results (MM) are made in Figs. 3.5-3.8, for the square plate shown in Fig. 3(b). The direct edge wave (EW) as given by Equations 3.5 and 3.6 is also plotted so that the effect of the corner diffracted fields is better illustrated. Note that in Fig. 3.7 (where  $\phi = 45^\circ$ ) the edge wave edge diffracted fields should be also added to the corner diffracted fields. The dipole is placed in the close vicinity of one of the edges ( $\rho' = 0.01\lambda$ ) of the plate and sufficiently far from its corners ( $s'_c \geq 2\lambda$ ). The agreement is good, especially in regions where contributions from other diffraction mechanisms other than the corner adjacent to the guiding edge are known to be negligible. In fact, as shown in Figs. 3.5-3.7, the agreement between the moment method data and the calculated field progressively improves for larger values of the  $\phi$  angle. For  $\phi = 45^\circ$  (Fig. 3.7), other mechanisms such as diffraction from the remote corners of the square plate as well as double and triple edge diffraction may contribute significantly to the pattern. Our approximation also improves when the paraxial region is approached ( $\beta \rightarrow 0^\circ, 180^\circ$ ), where, as a matter of fact, the total field is stronger. The latter justifies the validity of the asymptotic analysis which resulted in the multiplication of two transition functions as well as the choice of the correction factor for the direct dipole field. Unfortunately, the  $\hat{\phi}$ -directed field does not exhibit an analogous agreement (Fig. 3.8), at lower azimuthal cuts, due mainly to the fact that the analysis did not include secondary mechanisms which, clearly, contribute significantly to the pattern of that polarization. However, the small angular variation of the pattern in Fig. 3.8, which is a typical  $\hat{\phi}$  component pattern for  $\phi > 90^\circ$ , indicates that the corner associated  $\hat{\phi}$ -directed fields are sufficiently weaker compared with the  $\hat{\phi}$  component of the direct edge wave and can be neglected in practical calculations.

The results also reveal a small variation of the total field with respect to the azimuthal coordinate (angle  $\phi$ ), in contrast with the relative large changes of the calculated pattern in the elevation plane. The  $\phi$  dependence becomes significant only at lower cuts where the contribution from the opposite edge and its two adjacent corners is appreciable.

The second example examined involves also the radiation of a small monopole in the close vicinity of one of the edges of a rectangular plate, but now with different distances from its corners. The geometry of this monopole-rectangular plate configuration is depicted in Fig. 3(c). The calculated field is compared again with moment method results as well as measured data, as shown in Figs. 3.9 and 3.10 in the azimuthal planes  $\phi = 180^\circ$  and  $\phi = 150^\circ$ , respectively. The accuracy of the measured data deteriorated in smaller azimuthal angles, where the support structure influenced significantly the measured radiation pattern. In Fig. 3.9, an absorbing material has been placed around the remote corners and the opposite edge of the rectangular plate, so that their effect in the total pattern is reduced. Clearly, the agreement is better in this case (Fig. 3.9), in contrast with the results of Fig. 3.10 where the ram was removed.

It should be noted that neither the "Physical Optics" solution nor the equivalent current formulation are expected to yield accurate results for small angular sector angles ( $\alpha \ll \pi/2$ ). In this case a strong coupling between the two edges forming the sector occurs, which is not encountered in the evaluation of the radiation integral of the currents flowing along the edge (1). Moreover, when  $\alpha \rightarrow \pi$ , the Physical Optics corner diffracted field vanishes and the total solution reduces to the edge wave over an infinite wedge, whereas the same property is not true for the equivalent current formulation of the vertex diffracted field. The latter, therefore, fails in cases of very wide angles, which require a more careful treatment.

### 3.6 Conclusions

The major objective of this study was to describe approximately the edge wave diffraction mechanisms associated with the interaction of an edge wave and the vertex of a trihedron as a first step to the approximation of more complex geometries. A dipole radiating in the close vicinity of one of its edges produces an edge wave which behaves essentially as a ray optical field in the vicinity of the vertex. To approximate the vertex diffracted wave a UTD solution was developed based on a Physical Optics like approach to defining the currents. The addition of a fringe current component flowing in the vicinity of the terminating edges, yields a continuous radiation pattern across the shadow boundaries of the edge diffracted waves. Although, the

approach is neither rigorous nor complete from a PTD point of view, cast in UTD form, it yields comparable results with moment method as well measured data and can be used as a first engineering approximation to the edge wave edge and vertex diffraction problems.

This method can be possibly extended to the examination of the double corner and corner to edge edge wave diffraction mechanisms, with several practical applications. The latter, being also a possible extension of the present GTD, so that it may incorporate higher order diffraction mechanisms, awaits future work.

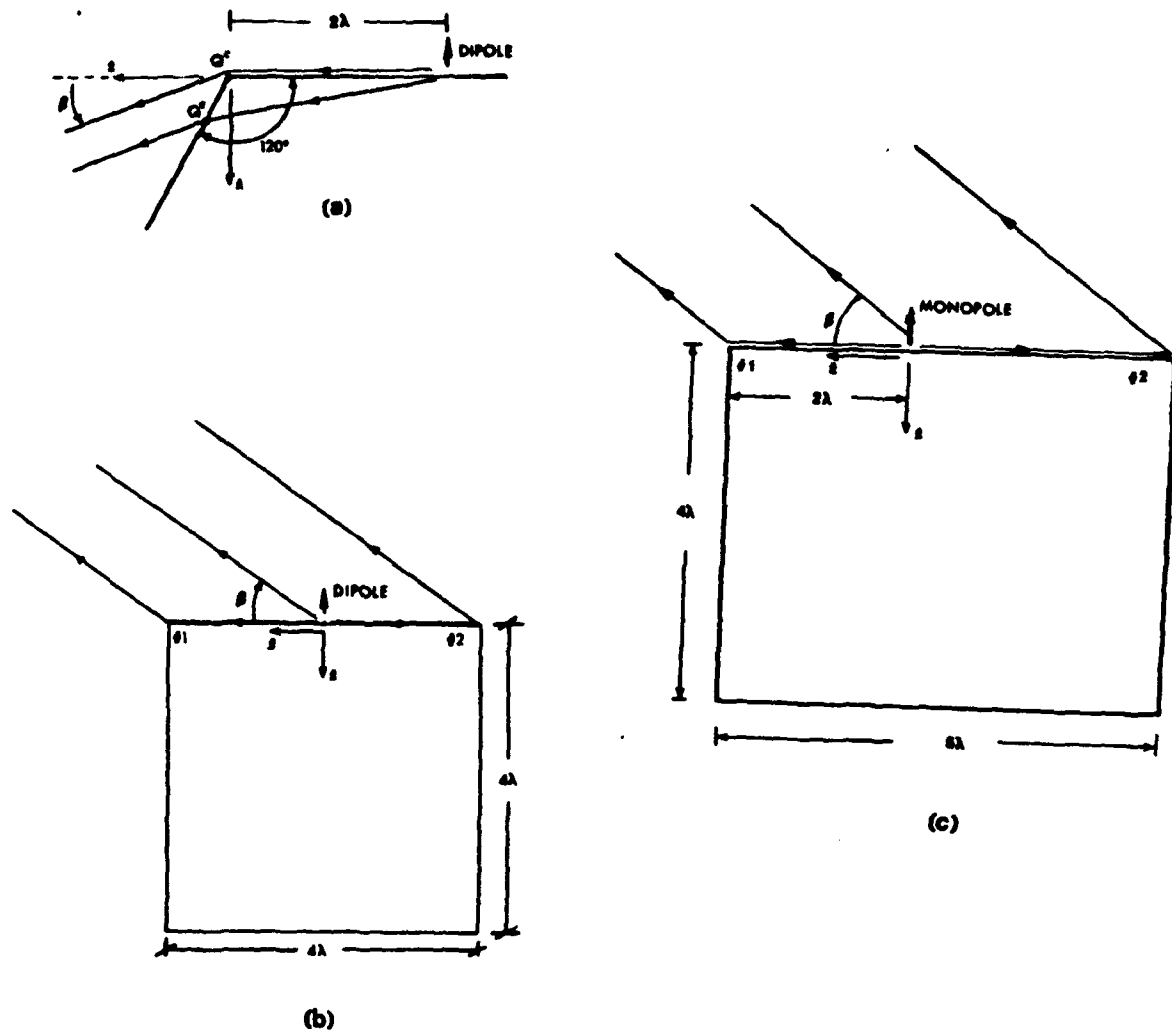


Figure 3.3: Flat plate geometries examined for the comparison of the calculated field with moment method and measured data: (a) Angular sector, (b) Square plate with the dipole in the center of one of its edges, (c) Rectangular plate with the dipole at unequal distances from the adjacent corners.

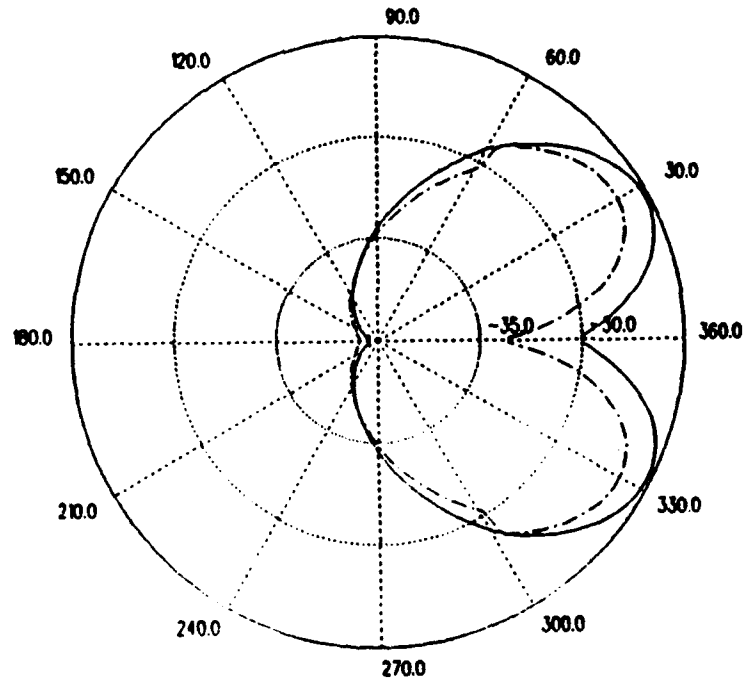


Figure 3.4: Far region edge and vertex diffracted  $\hat{\beta}$ -directed field for the angular sector geometry of Fig. 3(a) at the cone  $\beta = 85^\circ$ .

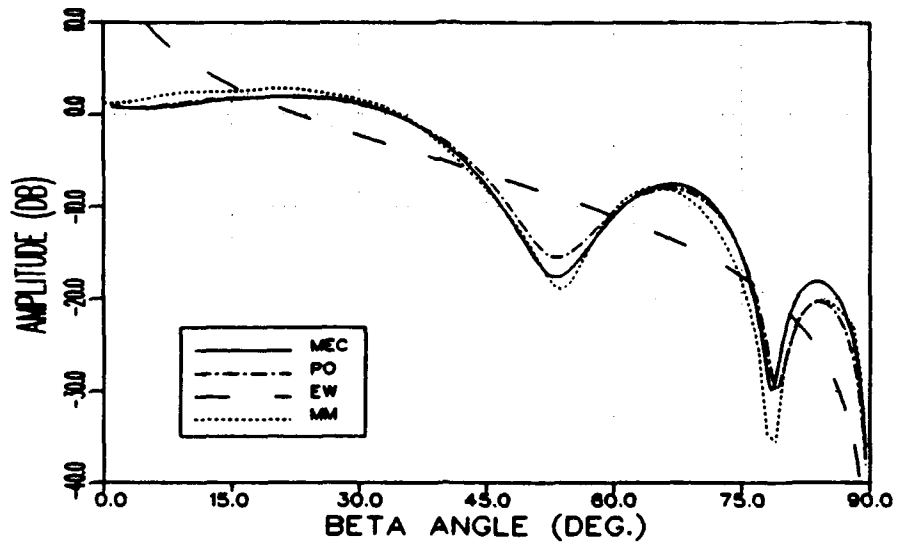


Figure 3.5: Far field  $\hat{\beta}$ -directed wave radiated by the dipole of Fig. 3(b) at the azimuthal cut  $\phi = 180^\circ$ .

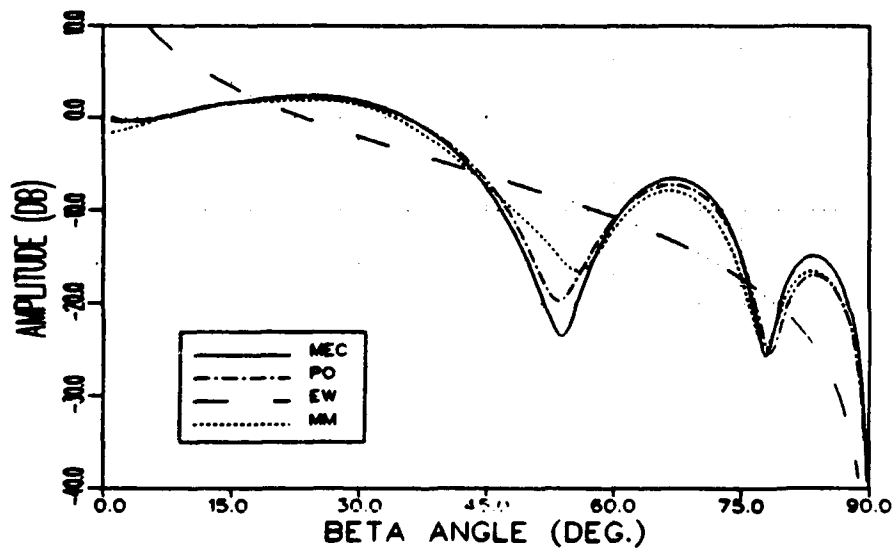


Figure 3.6: Far field  $\hat{\beta}$ -directed wave radiated by the dipole of Fig. 3(b) at the azimuthal cut  $\phi = 135^\circ$ .

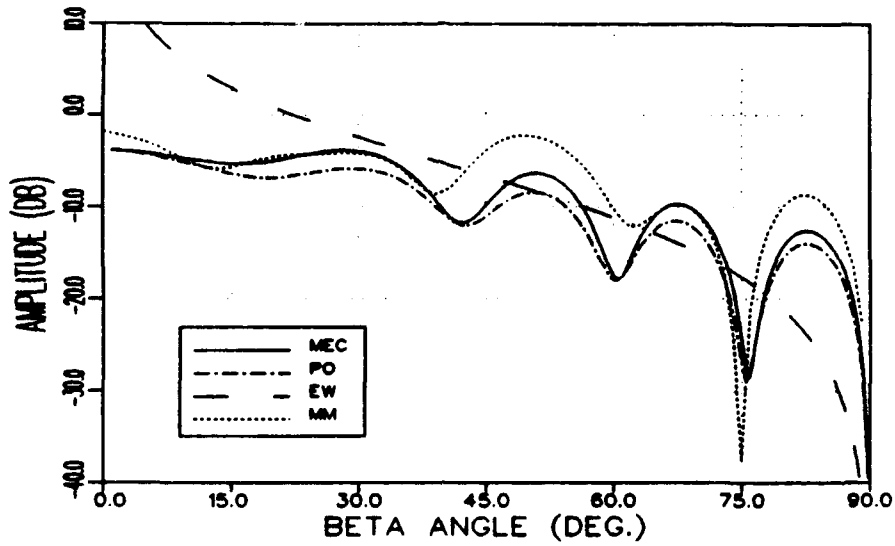


Figure 3.7: Far field  $\hat{\beta}$ -directed wave radiated by the dipole of Fig. 3(b) at the azimuthal cut  $\phi = 45^\circ$ .

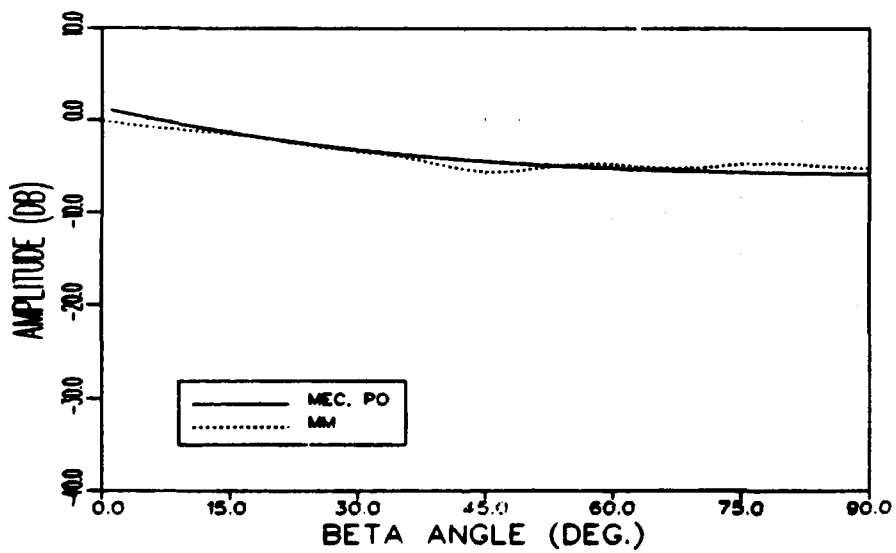


Figure 3.8: Far field  $\hat{\phi}$ -directed wave radiated by the dipole of Fig. 3(b) at the azimuthal cut  $\phi = 120^\circ$ .

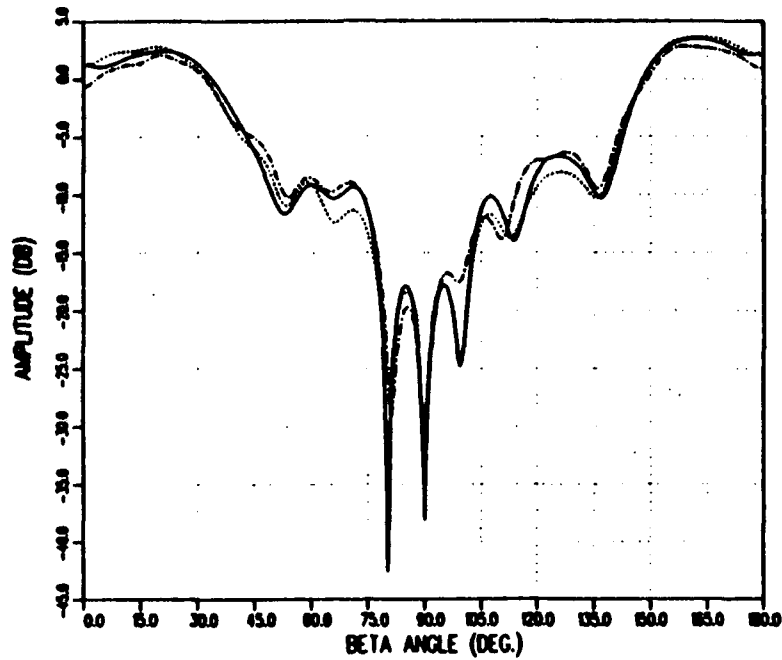


Figure 3.9: Far field  $\hat{\beta}$ -directed wave radiated by the dipole of Fig. 3(c) at the azimuthal cut  $\phi = 180^\circ$ . *Solid line: Calculated field, Dashed line: Measured field, Dotted line: Moment method solution.*

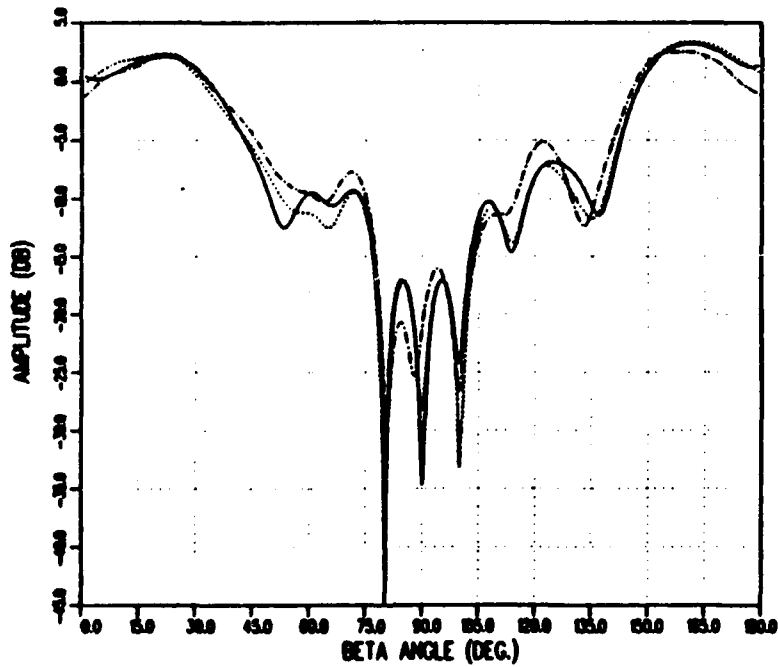


Figure 3.10: Far field  $\hat{\beta}$ -directed wave radiated by the dipole of Fig. 3(c) at the azimuthal cut  $\phi = 150^\circ$ . *Solid line: Calculated field, Dashed line: Measured field, Dotted line: Moment method solution.*

## Chapter 4

### Summary

This report summaries two theoretical studies pertaining to the scattering from flat plate structures. A new far zone corner diffraction coefficient has been developed and tested against existing solutions, method of moments, and measurements. It has been shown to be very useful and accurate for backscatter and especially for bistatic scattering where many of the previous methods give less accurate results. A new method for determining an edge wave - vertex diffraction coefficient for source excitation has also been developed. It is tested against method of moments and measurements with excellent results. This is an intermediate step for determining a far zone edge wave solution for which preliminary results are being tested.

# Bibliography

- [1] T. J. Brinkley and R. J. Marhefka, "Far zone bistatic scattering from flat plates," Technical Report 718295-8, The Ohio State University ElectroScience Laboratory, Department of Electrical Engineering, July 1988. Prepared under Contract No. F33615-86-K-1023 for Wright Patterson Air Force Base.
- [2] L. P. Ivriissimtzi and R. J. Marhefka, "Edge wave edge and vertex diffraction," Technical Report 718295-9, The Ohio State University ElectroScience Laboratory, Department of Electrical Engineering, July 1988. Prepared under Contract No. F33615-86-K-1023 for Wright Patterson Air Force Base.
- [3] F. A. Sikta, W. D. Burnside, T. T. Chu, and L. Peters, Jr., "First-order equivalent current and corner diffraction scattering from flat plate structures," *IEEE Trans. Antennas Propagat.*, vol. AP-31, pp. 584-589, July 1983.
- [4] A. Michaeli, "Elimination of infinities in equivalent edge currents, Part I: fringe current components," *IEEE Trans. Antennas Propagat.*, vol. AP-34, pp. 912-918, 1986.
- [5] E. H. Newman and R. L. Dilsavor, "A user's manual for the electromagnetic surface patch code: ESP Version III," Technical Report 716148-19, The Ohio State University ElectroScience Laboratory, Department of Electrical Engineering, May 1987.
- [6] A. C. Ludwig, "Backscattering from a cube," *Applied Computational Electromagnetic Society Journal and Newsletter*, vol. 2, pp. 55-73, Fall 1987.

- [7] R. Tiberio, M. Giuliano, G. Pelosi, and R. G. Kouyoumjian, "High-frequency electromagnetic scattering of plane waves from double wedges," To be published.
- [8] F. A. Sikta and L. Peters, Jr., "UTD analysis of electromagnetic scattering by flat plate structures," Technical Report 711930-2, The Ohio State University ElectroScience Laboratory, Department of Electrical Engineering, 1981.
- [9] R. J. Marhefka and W. D. Burnside, "Numerical electromagnetic code - basic scattering code (version 2), Part I: user's manual," Technical Report 712242-14, The Ohio State University ElectroScience Laboratory, Department of Electrical Engineering, Dec. 1982. Prepared under Contract No. N00123-79-C-1469 for Naval Regional Contracting Office.
- [10] E. H. Newman and R. J. Marhefka, "An overview of MM and UTD methods at The Ohio State University," To be published in special issue on RCS in Proc. of IEEE.
- [11] P. Y. Ufimtsev, "Method of edge waves in the physical theory of diffraction," Tech. Rep. Document ID No. FTD-HC-23-259-71, Air Force Systems Command Foreign Tech. Div., 1971. (Translation from the Russian "Method Krayevykh voln v fizicheskoy teorii difraktsii," Soviet Radio Publication House, Moscow, 1962).
- [12] J. B. Keller, "Geometrical theory of diffraction," *J. Opt. Soc. of America*, vol. 52, pp. 116-130, Feb. 1962.
- [13] R. G. Kouyoumjian and P. H. Pathak, "A uniform geometrical theory of diffraction for an edge in a perfectly conducting surface," *Proc. IEEE*, vol. 62, pp. 1448-1461, 1974.
- [14] C. E. Ryan, Jr. and L. Peters, Jr., "Evaluation of edge-diffracted fields including equivalent currents for the caustic regions," *IEEE Trans. Antennas Propagat.*, vol. AP-7, pp. 292-299, 1969.
- [15] A. Michaeli, "Equivalent edge currents for arbitrary aspects of observation," *IEEE Trans. Antennas Propagat.*, vol. AP-32, pp. 252-258, 1984.

- [16] K. M. Mitzner, "Incremental length diffraction coefficients," Tech. Rep. No. AFAL-TR-73-296, Northrop Corp., Aircraft Division, Apr. 1974.
- [17] E. F. Knott, "The relationship between Mitzner's ILDC and Michaeli's equivalent currents," *IEEE Trans. Antennas Propagat.*, vol. AP-33, pp. 112-114, 1985.
- [18] P. Y. Ufimtsev and D. I. Butorin, "Explicit expressions for an acoustic edge wave scattered by an infinitesimal edge element," *Sov. Phys. Acous.*, vol. 34, pp. 283-287, July-August 1986.
- [19] P. Y. Ufimtsev, "A new mathematical formulation of the physical theory of diffraction," Submitted for publication.
- [20] O. M. Buyukdura, R. J. Marhefka, and W. Ebihara, "Radar cross section studies, Phase III," Technical Report 716622-1, The Ohio State University ElectroScience Laboratory, Department of Electrical Engineering, Apr. 1986. Prepared under Contract No. NO429A-84-C-0363 for Pacific Missile Test Center.
- [21] W. B. Gordon, "Far-field approximations to the Kirchoff-Helmholtz representations of scattered fields," *IEEE Trans. Antennas Propagat.*, pp. 590-592, July 1975.
- [22] O. M. Buyukdura. Personal communication.
- [23] A. K. Dominek. Personal communication.
- [24] L. Krauss and L. M. Levine, "Diffraction by an elliptic cone," *Commun. Pure Appl. Math.*, vol. XIV, pp. 49-68, 1961.
- [25] R. S. Satterwhite and R. G. Kouyoumjian, "Electromagnetic diffraction by a perfectly conducting plane angular section," Tech. Rep. 2183-2, The Ohio State University ElectroScience Laboratory, Department of Electrical Engineering, 1970.
- [26] R. G. Kouyoumjian, P. H. Pathak, and W. D. Burnside, "A uniform GTD for the diffraction by edges, vertices and convex surfaces," in

*Theoretical Methods for Determining the Interaction of Electromagnetic Waves with Structures*, (J. K. Skwirzynski, ed.), pp. 497-561, Sijthoff and Noordhoff, 1981.

- [27] O. M. Buyukdura, *Radiation from Sources and Scatterers Near the Edge of a Perfectly Conducting Wedge*. PhD thesis, Ohio State University, Department of Electrical Engineering, 1984.
- [28] J. Meixner, "The behavior of electromagnetic waves at edges," *IEEE Trans. Antennas Propagat.*, vol. AP-20, pp. 442-446, 1972.
- [29] A. Michaeli, "Elimination of infinities in equivalent edge currents, Part II: physical optics components," *IEEE Trans. Antennas Propagat.*, vol. AP-34, pp. 1034-1037, 1986.
- [30] M. Abramowitz and I. A. Stegun, eds., *Handbook of Mathematical Functions*. Dover Publications, 1970.
- [31] I. S. Gradshteyn and I. M. Ryzhik, *Table of Integral, Series, and Products*. Academic Press, Inc., 1980.
- [32] P. H. Pathak and R. G. Kouyoumjian, "A dyadic diffraction coefficient for a perfectly conducting wedge," Technical Report 2183-4, The Ohio State University ElectroScience Laboratory, Department of Electrical Engineering, 1970.